Cloud Regimes Over the Amazon Basin: Perspectives From the GoAmazon2014/5 Campaign

Scott E. Giangrande[1], Dié Wang[1], and David B. Mechem[2]

[1]Environmental and Climate Sciences Department, Brookhaven National Laboratory, Upton, NY, USA
[2]Department of Geography and Atmospheric Science, University of Kansas, Lawrence, Kansas, USA

Correspondence to: Scott E. Giangrande (sgrande@bnl.gov)

Abstract. Radiosonde observations collected during the GoAmazon2014/5 campaign are analyzed to identify the primary thermodynamic regimes accompanying different modes of convection over the Amazon. This analysis identifies five thermodynamic regimes that are consistent with traditional Amazon calendar definitions of seasonal shifts, which include a wet, transitional, and three dry-season regimes based on a k-means cluster analysis. A multisensor ground-based approach is used to project associated bulk cloud and precipitation properties onto these regimes. This is done to assess the propensity for each regime to be associated with different characteristic cloud frequency, cloud types, and precipitation properties. Additional emphasis is given to those regimes that promote deep convective precipitation and organized convective systems. Overall, we find reduced cloud cover and precipitation rates to be associated with the three dry regimes and those with the highest convective inhibition. While approximately 15% of the dataset is designated as organized convection, these events are predominantly contained within the transitional regime.

1 Introduction

A primary source of uncertainty in global climate or earth system model (GCM, ESM) predictions of possible climate change is the representation of cloud processes and associated cloud feedbacks that regulate Earth's energy and water cycles (e.g., Klein and Del Genio, 2006; Del Genio, 2012). One explanation for continuing deficiencies in climate model cloud-process representations points to uncertainties in how deep convection is parameterized. Unfortunately, the assumptions underpinning the parameterizations are often poorly constrained by observations. Formulating well-behaved convective parameterizations necessitates routine cloud observations, married to their associated meso- and synoptic-scale controls, and collected over the variety of global convective regimes. Untangling these cloud–climate controls in ways suitable to ongoing model development demands long-term, multi-scale, multi-sensor observations that often require challenging instrument deployments to capture cloud and precipitation properties in remote and under-sampled global regimes (e.g., Louf et al., 2019).

As home to the largest tropical rainforest on the planet, the Amazon basin experiences prolific and diverse cloud conditions that vary according to pronounced changes in seasonal regimes. However, these clouds, regimes and their associated convective intensity are interconnected, with cloud properties (coverage, depth, precipitation) strongly influenced by (and

1

influencing, via feedbacks) seasonal shifts in the thermodynamic forcing, as well as larger-scale atmospheric Hadley and Walker circulation variability (e.g., Fu et al., 1999; Machado et al., 2004; Misra, 2008). Recently, the ongoing struggle of GCMs and weather prediction models to represent aerosols, clouds and their interactions over this expansive tropical area motivated the 2-year US Department of Energy (DOE) Atmospheric Radiation Measurement (ARM) Observations and Modeling of the Green Ocean Amazon (GoAmazon2014/5) campaign (e.g., Martin et al., 2016; 2017). As part of this effort, ARM deployed its Mobile Facility (AMF; e.g., Miller et al., 2014) downstream of Manaus, Brazil in the central Amazon. The facility enabled capture of the thermodynamic state, aerosol, cloud and precipitation properties in this location, through the deployment of multiple surface state and atmospheric profiling facilities (e.g., Mather and Voyles, 2013).

We classify the primary thermodynamic regimes that are associated with the cloud observations over Manaus using a k-means cluster analysis applied to the morning radiosonde launches collected during the GoAmazon2014/5 campaign. This is done to isolate the potential controls of large-scale conditions on convective regimes. Conceptually, this technique follows previous tropical clustering efforts such as Pope et al. (2009a, b) to examine the variability found in the North Australia monsoonal seasons. Their motivations were to promote objective methods to identify key monsoonal changes and establish cloud–precipitation regimes to evaluate the representation of these processes in global models (e.g., May and Ballinger, 2007). A similar opportunity is expected for Amazon studies, hinted at by several recent efforts (Marengo et al., 2017; Wright et al., 2017; Sena et al., 2018) that illustrate the complex cloud processes and the possible changing nature of yearly transitions from dry and rainy seasons in the Amazon. The clustering approach may also yield an improved understanding of the relationship between the intraseasonal variability and the different Amazon convective regimes (Betts et al., 2002; Ghate and Kollias 2016), as well as new insights into shallow-to-deep cloud transitions and model treatments therein (e.g., Khairoutdinov and Randall, 2006; Wu et al., 2009; Hohenegger and Stevens, 2013; Zhuang et al., 2017; Zhuang et al., 2018; Mechem and Giangrande 2018; Chakraborty et al., 2018; Chakraborty et al., 2020). Moreover, there is continuing need to identify particular seasonal, environmental or aerosol controls on Amazon convection and its intensity (Greco et al., 1990; Williams et al., 2002; Alcântara et al., 2011; Fan et al., 2018; Wu and Lee, 2019; Rehbein et al., 2019).

The proposed regime segregations are projected onto the large-scale synoptic patterns, forcing datasets, and remote-sensing cloud/precipitation observations for the GoAmazon2014/5 campaign. Although there are limitations when drawing conclusions from any two-year campaign dataset, these efforts are used to assess possible controls and convective-cloud predictors as related to i) the interpretation and consistency of these radiosonde clusters with previous wet/dry seasonal definitions for the Amazon, ii) bulk regime relationships to particular cloud presence/absence, the iii) precipitation properties for these regimes to include diurnal cycles, and iv) the propensity for regimes to promote extremes in precipitation such as null-event days or mesoscale convective systems (MCSs, Houze, 2004; Wang et al., 2019; Wang et al., 2020). The GoAmazon2014/5 datasets are briefly described in section 2. The clustering algorithm, displays of the regimes according to thermodynamic variability, and additional methodology sensitivity testing are described in sections 2 and 3. Section 3 also

explores the relationships between these regimes and overarching synoptic patterns, as well as area-averaged and observationally constrained vertical profiles (e.g., horizontal moisture convergence) often used to force single-column models (SCMs). Summaries of cloud properties associated with these regimes are found in section 4. This includes discussion on the propensity for the regimes to promote precipitation, and the likelihood of MCS events initiating nearby the campaign facilities. Finally, key findings for this study are summarized in section 5.

2 GoAmazon2014/5 Dataset and Processing Methods

Datasets for this study were collected by the U.S. DOE ARM facility during its "Observations and Modeling of the Green Ocean Amazon 2014–2015" campaign near Manaus, Brazil from January 2014 through December 2015 (herein, GoAmazon2014/5 or MAO; Martin et al., 2016; 2017; Giangrande et al., 2017). The primary datasets were from the routine ARM radiosonde launches during the campaign at the "T3" main AMF field site downwind of the city of Manaus, Brazil and near Manacapuru, Brazil. These radiosondes provide the thermodynamic quantities of interest and act as basis for regime clustering methods (section 2.2).

2.1 ARM GoAmazon2014/5 Products and Datasets

Details on ARM radiosondes, their preprocessing and convective parameter estimates, follow previous ARM studies (e.g., Jensen et al., 2015). The quantities of interest for this study include estimates of the convective available potential energy (CAPE), the convective inhibition (CIN), the Relative Humidity (RH) at low- (surface to 3 km), mid- (3 km to 6 km) and high-levels (above 6 km) of the atmosphere, the 0–5-km wind shear, the Level of Free Convection (LFC), the Lifting Condensation Level (LCL), and the 0–3-km Environmental Lapse Rate (ELR). Our CAPE calculations follow a traditional parcel theory approach (condensation/evaporation of water vapor only, assuming irreversible parcel ascent in a virtual potential temperature framework, e.g., Bryan and Fritsch, 2002). The originating parcels for CAPE/CIN estimates are defined by the level of the maximum virtual temperature in the lowest kilometer (below 700 hPa). Thus, the standard calculations for CAPE and CIN represent the most buoyant parcel in the boundary layer such that the reported values are comparable to 'most unstable CAPE/CIN' (herein, MUCAPE/MUCIN). Mixed-layer CAPE and CIN estimates (mean parcel properties over the lowest 500 m, which we take to be representative of the mixed layer) were also computed for comparison.

Cloud properties were collected by collocated instruments at the MAO site, with additional information provided by observationally-constrained reanalysis datasets. For precipitation properties, surveillance S-band (3 GHz) radar observations were available to within 70 km of the MAO site as collected by the System for the Protection of Amazonia (SIPAM) radar located on the south end of Manaus (e.g., Ponta Pelada airport, Martin et al., 2016). These radar data were calibrated against

satellite measurements, and subsequently gridded to a 2 km × 2 km horizontal grid at 2 km AGL (e.g., Schumacher and Funk, 2018).

105 Cluster routines incorporate only the morning (1200 UTC, 0800 local time) radiosondes that are launched in clear conditions. Clear conditions are defined as those having no rainfall at the MAO site according to rain gauge measurements to within an hour of launch time. Confirmation of precipitation-free conditions was also performed using SIPAM observations and manual checks for contaminated radiosondes. A more restrictive precipitation constraint (i.e., no rainfall at the gauge site between 0900 UTC and 1200 UTC) did not result in an appreciable change to the results that follow. A motivation for using the morning

110 radiosonde was to capture pre-convective cloud conditions prior to the daily transition from clear skies to shallow cumulus to deep convection, given previous studies on the diurnal precipitation cycle for Manaus that peaks after local noon (e.g., Adams et al., 2013; Tanaka et al., 2014; Giangrande et al., 2017). Additional concerns are that earlier (0600 UTC) or later (1800 UTC) radiosonde launches are not representative of the pre-convective environment, and are more susceptible to existing clouds, overnight fog (e.g., Anber et al., 2015), precipitation and/or cold pool contamination. In total, 607 daily radiosondes from the

115 campaign (out of 696, 12-UTC radiosondes in total) met these criteria, with 27 days removed due to missing radiosondes. Of the days flagged as contaminated or 'missing' at 1200 UTC, approximately 30-40 days were associated with radar-designated MCSs passing over MAO (section 4).

Time-height (column) cloud properties are provided by a hybrid cloud radar / radar wind profiler (RWP) product developed

120 during GoAmazon2014/5 (Giangrande et al., 2017; Feng and Giangrande, 2018). The product combines the ARM multi-sensor (e.g., cloud radar, lidar, ceilometer, radiometer) Active Remote Sensing of CLouds (ARSCL; Clothiaux et al., 2000) cloud boundary designations with collocated 1290 MHz ultra-high frequency (UHF) RWP measurements (e.g., Giangrande, 2018; Wang et al., 2018), and gauge observations. The RWP improves the ARSCL cloud-boundary estimates of cloud echo top by sampling deeper precipitating clouds that otherwise attenuate/extinguish the cloud radar beam. A simple cloud-type

125 classification is performed following McFarlane et al. (2013) and Burleyson et al. (2015). Observed clouds are classified into seven categories according to the height of the cloud and cloud thickness (Supplemental Table S1). These seven cloud categories are 'shallow', 'congestus', 'deep convection', 'altocumulus', 'altostratus', 'cirrostratus/anvil', and 'cirrus'.

Large-scale synoptic perspectives on the regimes are obtained using reanalysis fields from ERA5 (Hersbach and Dee, 2016)

130 and the ARM variational analysis product (ARM-VARANAL). The VARANAL is derived from ECMWF analysis fields and ARM observations during GoAmazon2014/15 using the constrained variational analysis method of Zhang and Lin (1997). The product is available at 3-hour intervals on a regular vertical grid of 25 hPa over a domain of ~110 km radius around the MAO site (Xie et al., 2014; 2016). The product is also constrained by the domain-mean precipitation as observed by the SIPAM radar. Additional details on these products during GoAmazon2014/5 are found in Tang et al. (2016).

135

2.2 *K*-means Clustering Methods

Regime classification is accomplished using an open-source Scikit-learn's *k*-means algorithm applied to input radiosonde observations (toolkit from Pedregosa et al., 2011). The choice of *k*-means solutions over other configurations is done for simplicity and is consistent with previous radiosonde applications. While the sensitivity of proposed regime designations to different clustering approaches is not the subject of this study, applying alternate configurations did not alter relative clusters or composite interpretations.

One property of *k*-means clustering is that the number of clusters needs to be prescribed. One expectation from the Amazon convective literature (e.g., Williams et al., 2002) is that three to four regimes account for the bulk seasonal thermodynamic variability: i) a 'wet' season regime typically defined as December through April, ii) a 'dry' season regime from June through September, and iii) one or two 'transitional' regimes associated with the months leading into the wet and dry regimes, respectively. However, calendar definitions of the regimes vary in the literature (e.g., Zhuang et al., 2017), which may cause additional confusion when interpreting the findings across studies. From sensitivity testing (see section 2.3), we establish the number of clusters at five. Radiosonde temperature, dew point temperature and zonal/meridional wind information are input at 20 equally-spaced levels from 1000 hPa to 200 hPa, as similar to previous applications over Northern Australia (Pope et al., 2009a,b). This input resolution is coarser than the resolution of both the ARM radiosondes (~2 hPa), and that of the 25-hPa VARANAL resolution. Additional tests (not shown) indicate that, for this particular case, the *k*-means solutions are insensitive to improvements in the input radiosonde resolution (to the 2 hPa level), or input ordering of the data. Although the results for this study present cluster solutions that do not use standardized inputs (e.g., scaling all inputs to having a similar range, standard deviation), it is common practice in recent studies to scale inputs. Subsequent sections will comment on potential changes in cluster results when scaled inputs are substituted.

Figure 1 shows the cluster classification according to calendar-based Amazon definitions for the wet, dry and transitional seasons. The dry season months (Figure 1, bottom left panel) are predominantly associated with regimes 1-3, while the traditional Amazon wet season months (Figure 1, top right panel) are associated with regimes 4 and 5, with negligible contributions from the remaining regimes. The ambiguous transitional season (here, reflecting the months of May, October and November) indicates contributions from all regimes, though skewed towards regimes 4 and 5.

In Figure 2, we plot the time-series of regime designations throughout the campaign (top panel), with the associated monthly breakdowns for the clusters (bottom panel). Qualitatively, the temporal coherence of the individual clusters in the five-regime solution provides initial confidence in the appropriateness of this regime breakdown. Instances of regimes 4 and 5 are aligned with classical transitional and wet season periods, respectively, with regime 4 periods adjacent to regime 5 and not sporadically distributed within other regimes. The remaining clusters are interwoven within Amazon drier months. The observed cycling

5

170   between these dry clusters is of immediate interest, as this variability may be indicative of intraseasonal synoptic pattern phases in the dry season.

The specifics of the GoAmazon2014/5 campaign and its particular representativeness in the context of historical Amazon records should be considered when assessing cluster appropriateness. As summarized by Marengo et al. (2017), climatological

175   wet season onset for Manaus based on rainfall records is typically mid-November (e.g., Liebmann and Marengo, 2001). Their efforts indicate that traditional rainfall-based criteria and additional wet season onset measures such as outgoing longwave radiation indicators (e.g., Kousky, 1988) imply that the 2014-2015 wet season onset date occurred much later in the season (e.g., end of January, 2015). One explanation for the late onset, offered by Marengo et al. (2017), was that precipitation - the obvious indicator for wet-season onset -- was heavily influenced by the strengthening of the Madden–Julian Oscillation (MJO;

180   Madden and Julian, 1994) and associated influences on Amazon rainfall. Based on cluster outcomes in Figure 2, we did not identify a prolonged cluster arguably associated with a presumed 'wet season' condition (e.g., regime 5) until early December 2014. This coherent shift in the frequency of radiosonde regime 5 designations coincides with an extended change-over in the upper-level winds, as also shown in campaign thermodynamic summary plots (e.g., Fig. 2 from Giangrande et al., 2017). Nevertheless, we record multiple instances of regime 5 as early as November 2014, coinciding with a pronounced dry-to-wet

185   seasonal shift towards a deep-layer profile moisture (RH, see also Fig. 2, Giangrande et al., 2017). As before, the motivation for the k-means cluster method is not to 'pinpoint' an exact rainy season onset date (e.g., first appearance of a given cluster), rather to identify atmospheric regimes that may provide guidance towards subsets of attendant environmental conditions conducive to different bulk cloud properties.

190   **2.3 Additional *k*-means Cluster Sensitivity Considerations**

Establishing the number of clusters within *k*-means methods requires sensitivity testing. Too few clusters tends to overgeneralize and produce overly large intra-cluster variability; too many clusters lead to difficulty in interpretation, because there may be no physically meaningful distinction between clusters. Similar to justifications proposed by Pope et al. (2009a,

195   b), we are interested in regimes associated with significant radiosonde variability, and therein, potential relationships to cloud variability. One criterion Pope et al. (2009a,b) recommended was that each cluster account for no less than 10% of the dataset. When adopting this approach, Amazon solutions having more than five clusters generated additional clusters that accounted for fewer than 10% of the days.

200   When considering a six-cluster solution (supplemental Figure S1), the solution further subdivided the three drier regime clusters into four. However, the distinct separation between our wet (regime 5) and transitional (regime 4) clusters showed little difference when the number of clusters was increased from five to six. To be discussed in section 3, the wet and transitional regime separations predominantly differ from each other in their zonal/meridional wind structures. This does not

suggest that there are not specific differences depending on whether the transition is wet-to-dry and dry-to-wet, only that these differences are not as pronounced as the drier intraseasonal shifts. In contrast, the four-cluster solution meets our basic criterion for determining the number of clusters (Supplemental Figure S2). However, with only four clusters, the regime 4 and 5 clusters are combined into a single, deep-moisture profile regime. We demonstrate in later sections that the 5-regime clustering is able to delineate useful details in convective transitions and organization compared to the 4-regime solution. Because of this, the authors settle on the five-cluster solution as it maintains a separate transitional regime that the authors believe is consistent with the literature.

3 Thermodynamic and Large-Scale Interpretation of Amazon Regime Clusters

3.1 Composite Regime Thermodynamic Profiles and Parameter Displays

In Figure 3, we plot the composite radiosondes for all five regimes classified in the previous section. Shaded regions provide reference to composite radiosonde MUCAPE (red shading) and MUCIN (blue shading). Values reported on these images are the median values of the MUCAPE/MUCIN calculated for each individual sounding. The probability density plots in Figure 4 report the median values, distribution, quartiles and $10^{th}/90^{th}$ percentile extremes for the convective parameters of interest calculated from the radiosondes. Differences in MUCAPE and MUCIN across the regimes are largely driven by differences in the mid-to-upper level moisture / dew point temperature rather than temperature, a result consistent with the understanding that horizontal temperature gradients over the tropics are small, and variability in tropical convection is predominantly associated with horizontal moisture gradients ("weak temperature gradient approximation," Sobel et al., 2001). For all regimes, the standard deviations for MUCAPE and MUCIN parameters are similar (1100 J/kg and –15 J/kg, respectively). For other fields, the standard deviations vary with regime, with greater variability in the traditional dry season time frames than in the wet season. For example, standard deviation for wind shear is 4–6 m/s in the drier regimes and regime 4, versus 2–4 m/s in the wetter regime 5 conditions. For mixed-layer CIN, median regime values become less negative (from -85 J/kg for regime 1, to -33 J/kg for regime 5); however, the relative distribution and regime rankings are similar. When considering mixed-layer CAPE distributions, the values estimated for regime 1 (the highest MUCAPE regime) are noticeably smaller than the other regimes (median values dropping to 550 J/kg), whereas the remaining regimes all have similar median mixed-layer CAPE values of approximately 1000 J/kg (similar relative rankings otherwise). This discrepancy in mixed-layer CAPE and more prohibitive mixed-layer CIN may explain the absence of deep convection under regime 1 conditions (section 4).

Temporal patterns for regime 5 align with calendar wet season definitions and deeper moisture conditions. As visible in Figures 3 and 4, regime 5 is associated with reduced values for MUCAPE, but favorable (less negative) MUCIN to promote frequent convection (e.g., Giangrande et al., 2016). Regime 5 also records the lowest LFC and LCL heights, and reduced distribution

variability therein. Where regime breakdowns differ from traditional Amazon ideas is with these methods more frequently defining wet-to-dry season months such as April through June as 'transitional' regime 4 (Figure 3b) periods. As suggested by Figure 4f, the most significant difference we observe between the regime 4 and 5 composites are associated with profile winds, which includes increased lower-level wind shear in regime 4. A separation for wet and transitional regimes as according to wind shifts is consistent with ideas of transpiration or shallow convection 'preconditioning' an eventual wet season onset (e.g., Wright et al., 2017), e.g., favorable moisture conditions precede deeper cloud formation prior to regional scale wind shifts lending to wet season onset. However, this explanation would not apply for the reciprocal wet-to-dry transitional periods. Nevertheless, this dry-to-wet transition may bear some resemblance to the moistening and associated cumulus and congestus that occur as the MJO over the tropical western Pacific transitions from suppressed to active conditions (e.g., Johnson et al., 1999; Benedict and Randall, 2007; Mechem and Oberthaler, 2012, Zermeño–Díaz et al., 2015). Finally, while the differences in bulk wind shear are interesting between regimes 4 and 5, the magnitude of these differences are modest (to within 5 m/s). However, differences in mean shear within regime 4 may be indicative of differences in updraft structure (upright vs. tilted), convective cold pool circulations, and overall organization (e.g., Rotunno et al., 1988; Parker and Johnson, 2000; Weisman and Rotunno 2004).

Previous Amazon studies suggest that the dry-to-wet season transitional periods (e.g., September through November) are more conducive to storm electrification than wet-to-dry transitional periods (e.g., Williams et al., 2002). Our clusters do not distinguish differences between these periods (here, 'dry season' as traditionally defined, from June through September). Although the separations for regimes 1 (extreme dry) and 5 (extreme wet) are robust to our input tests, when k-means methods use standardized inputs, this change realigns five-cluster solutions towards 'pre' and 'post' dry season states (Supplemental Figure S3). While the authors did not pursue cluster solutions using standardized inputs for our primary examples, one suggestion is that standardized wind field inputs (to yield the same variability as the temperature and/or moisture fields) may help differentiate transitional periods. In our supplemental images, we provide composite properties for pre- (March through May) and post- (September through November) dry season regime 4 instances (supplemental Figure S4). Current regime 4 solutions exhibit enhanced MUCAPE for soundings collected during dry-to-wet periods that suggests those times as more conducive for vigorous updrafts (median MUCAPE values greater by ~700 J/kg).

The remaining clusters are associated with months traditionally classified as the Amazon dry season. Shifts between the three drier clusters are attributed to radiosonde mid-to-upper level moisture, with only minor controls associated with shifts in winds. Regime 1 is the least-frequently observed for the Amazon campaign, but the most significant outlier in terms of thermodynamic parameters (e.g., Figure 4). Regime 1 is also associated with the driest overall profile conditions (at low- and mid-levels), the lowest mixed-layer CAPE, the highest LFC, and the most prohibitive MUCIN conditions. Regime 3 favors humid conditions at the low-to-mid levels when compared to regimes 1 and 2, and larger values of mid-to-upper level humidity. The enhanced humidity at low- and mid-levels in Regime 3 may aid in initiation and maintenance of deep convection, while enhanced upper-

8

level humidity may promote saturated layers and ice-phase microphysical processes associated with stratiform precipitation. As widespread stratiform precipitation and MCSs have been reported also within the dry season (e.g., Wang et al., 2018; 2019), section 4 explores which dry season regime or regimes favor MCS.

275

3.2 Large-Scale Synoptic Conditions Projected into these Regimes

In Figure 5, we plot the means of the 1000-hPa geopotential height and wind field from the ERA5 (taken to represent the composite large-scale synoptic patterns) projected into each regime. Additional composites at the 200-hPa, 500-hPa and 850-
280   hPa levels are found in the supplemental materials (Supplemental S5-S7). For the wet regime (regime 5), the composites show land-ocean contrasts, and composites carry strong impressions of the Chaco low over the continent (and/or Bolivian high at the upper levels). Signatures of the Bolivian high are present in the deep layer of prevailing southerly winds over the MAO site and are exclusive to regime 5 (Figure 3e). Unlike other composites, regime 5 also suggests 1000-hPa flows providing moisture convergence into the Amazon basin originating from the tropical belt (northern tropical Atlantic, e.g., Drumond et
285   al., 2014), and associated calm or weak westerly low-level wind components over the MAO site. Although the 1200 UTC regime thermodynamic profiles did not indicate a pronounced difference between regimes 4 and 5 moisture characteristics, ERA5 composites suggest that regime 4 conditions are associated with different sources of moisture, with 1000-hPa winds over the Amazon basin shifting towards drier easterly zonal 1000-hPa flows. We speculate that the regime 4/5 shift visible in the large-scale composites may be associated with the positioning and strength of the South Atlantic Convergence Zone
290   (SACZ) and its influences on the Amazon basin during the wet season (e.g., Carvalho et al., 2004). Drier season regimes have transitioned to southerly low-level flow suggestive of drier, colder air reaching the central Amazon. These patterns vary according to the positioning and strength of offshore features that, in turn, funnel increasingly drier, colder air from the southeast (e.g., tropical South Atlantic; Drumond et al., 2014).

295   GoAmazon2014/5 datasets recorded one complete transition from the dry season to the wet season. In Figure 6, we plot the composite 1000-hPa patterns associated with regime 5, with each panel corresponding to a different monthly composite between October and January. Noting that October contained few instances of regime 5 conditions, composite ERA5 maps suggest large-scale trends and flow patterns were reminiscent of regime 4 (e.g., transitional) composites (Figure 5d), and with weak indications for a continental surface low pressure or moisture inbound from southward latitudes. December composite
300   patterns, in contrast, better reflect prevalent regime 5 composite behaviors (e.g., Figure 5e), that by January shift towards westerly low-level flow and are associated with low pressure and the SACZ. Westerly shifts in the central Amazon rainy seasons have been previously discussed as promoting a moist troposphere and frequent (albeit, not necessarily more intense) convection compared to easterly flow regimes near the beginning of the rainy season (e.g., Betts et al., 2002; Cifelli et al., 2002; Peterson et al., 2002).

305

To further explore attendant large-scale conditions and regime transitions, in Figure 7 we plot composite daily projections of horizontal moisture advection and vertical velocity from the VARANAL product. Estimated horizontal advection of moisture (e.g., $-V*\nabla q$; V is horizontal wind vector, q is water vapor mixing ratio; top row, green shading) is highest (positive) at the lower levels for the regime 4 and 5 clusters, and maximized at the lowest levels below 700-hPa around the 1200 UTC radiosonde launch time (dashed line). Note that the large-scale vertical velocity w (bottom row) is constrained by the domain-mean precipitation (assimilated SIPAM observations), with the strength of vertical motion adjusted by the diabatic heating derived from the SIPAM-estimated precipitation rates (e.g., Xie et al., 2014). Regimes with higher precipitation rates will indicate stronger ascending motion associated with greater diabatic heating during the afternoon precipitation periods. Interestingly, the large-scale w patterns during the morning hours are similar across regimes 2 through 5. Similarly, each regime indicates large-scale subsidence above 600-hPa that peaks around radiosonde launch time. However, regime 1 is an outlier and suggests substantial large-scale subsidence (above 600-hPa) and weak lower-level ascent around the morning radiosonde.

Finally, in Figure 8 we isolate the variational analysis profiles corresponding to the pre-convective radiosonde launches by plotting median profiles and 10th/90th percentile values at 1200 UTC. Regimes 4 and 5 share similar characteristics and enhanced moisture advection (lower levels) and larger-scale w in the mean and extremes (90th percentile). Regime 4 also displays stronger upward motions from near the surface to 650-hPa, and stronger extremes in w from ~750-hPa upward. Since 1200 UTC is prior to significant domain-mean precipitation (section 4.2), these enhancements in regime 4 motions are not influenced by precipitation constraints. Similarly, moist regimes lack the extreme negative (dry) moisture advection (10th percentile properties) found in regimes 1–3.

4 Regime Cloud and Precipitation Summaries, Likelihood for Precipitation Extremes

4.1 Cloud Frequency

Cumulative cloud frequency and diurnal summaries are plotted in Figure 9. Note, the 'all' examples in Figures 9f,g represent the summary dataset behaviors that include all days including those having precipitation at 1200 UTC. The characteristics are in-line with monthly breakdowns previously available for the GoAmazon2014/5 campaign as reported by Collow et al. (2016). In Figure 10, we plot the frequency of specific cloud types for the periods following 1200 UTC (radiosonde launch) to 0000 UTC, to include the relative frequency of null conditions over the site. For the frequency plots in Figure 10, multiple cloud layers can be identified in the same column; therefore, individual cloud types and null conditions do not add up to 100%.

Cloud properties in Figures 9 and 10 indicate regime 1 is least favorable for cloud coverage (total, or daytime hours following

340 the radiosondes). This is consistent with the least-favorable 1200 UTC convective parameters, moisture advection and subsidence as discussed in previous sections, as well as GoAmazon2014/5 dry-season studies on precipitation controls (e.g., Ghate and Kollias, 2016). During GoAmazon2014/5, regime 1 was the only regime where a majority of the daytime hours over the site were not populated with clouds (e.g., Figure 10b). When clouds were present, the most frequent cloud type was shallow cumulus ('shallow'). Upper-level cirrus clouds occupy a substantial fraction of the cloud observations under all

345 regimes, and are the second-most frequent clouds observed for regime 1 conditions. Presumably, the prevalence of cirrus in regime 1 is attributable to cirrus generated remotely then being advected over the site. Interestingly, Figure 9 suggests there is an absence of cirrus and other cloud types in the periods around the 1200 UTC radiosonde launch. This provides confidence that the 1200 UTC radiosondes used as the basis of regime classifications are not contaminated by clouds. All regimes suggest large-scale subsidence at upper levels around 1200 UTC (e.g., Figure 7), which may explain the absence of cirrus.

350

The drier cluster cloud summaries in Figures 9 and 10 indicate increasing cloudiness from regimes 1 to 3, with cloud frequency positively associated with reduced MUCIN (lower MUCAPE) and higher column RH. Dry-season cloud frequency (regimes 1-3), including mid (congestus)-to-upper level (anvil, to include widespread/deep stratiform shields) cloud frequency, is significantly lower than observed for regimes 4 and 5 (Figure 9g). Among the drier regimes, regime 3 conditions are most

355 conducive to clouds, although the relative cloud frequency as plotted in Figure 10 is similarly-scaled to the cloud types in regime 2. Moreover, diurnal cycles indicate that relative contributions from congestus are mostly absent from regime 1-3 mid-morning to afternoon periods (e.g., bimodal), and the increase in frequency between regimes 2 and 3 is attributed to enhanced shallow (echo tops < 3 km) and deeper (isolated) convection (echo tops > 8 km). There is weak evidence of overnight precipitating clouds during the dry season (e.g., Ghate and Kollias 2016), observed during the relatively moist regime 3.

360

MAO clouds are most frequently observed during the moist regimes (regimes 4 and 5), with increases in frequency attributed to contributions from all cloud types. Regime 5 indicates the highest frequency for shallow to mid-level clouds (e.g., 'shallow', 'congestus', and 'alto'), and the highest frequency overall as shown in Figure 9g. Diurnal plots suggest a gradual daytime shallow-to-deep cloud transition for regimes 4 and 5, consistent with previous arguments for increased water vapor in the

365 lower troposphere as the primary factor responsible for triggering this transition (e.g., Ghate and Kollias 2016). Interestingly, the bulk timing of this transition is potentially contingent on the regime, as this is apparently occurring later in the day according to regime 5 composites. One explanation for the delayed timing is that this transition may be slowed by the reduced incident solar radiation associated with more frequent shallow clouds under regime 5 or wet season conditions (e.g., Zhuang et al., 2017). Variations in shallow-to-deep timing are also consistent with differences in surface energy balance partitioning,

370 which are a strong function of soil moisture (e.g., Findell and Eltahir 2003a, b; Jones and Brunsell, 2009). Higher soil moisture values in the wet regime favor a partitioning of the surface net radiation toward more latent than sensible heat flux (i.e., smaller Bowen ratio). This partitioning leads to a wetter boundary layer, but weaker generation of turbulent boundary-layer growth

that should foster a slower transition. Even in a tropical rainforest, the importance of moisture availability has been shown to have a large impact on Bowen ratio (Gerken et al., 2018), suggesting this as a possible mechanism for modulating the onset of
375   deep convection.

Regime 5 indicates a trimodal distribution of convective clouds, as observed in previous tropical studies (e.g., Johnson et al., 1999). Over the tropical oceans, the congestus mode is associated with a mid-level stable layer near the melting (0°C) level (e.g., Johnson et al., 1999; Jenson and Del Genio 2006). This is thought to arise from radiative interactions accompanying
380   intrusions of dry air from poleward latitudes (e.g., Mapes and Zuidema 1996; Redelsperger et al., 2002; Pakula and Stevens, 2009) or melting processes in organized stratiform precipitation (Mapes and Houze, 1995), though recent findings argue that the melting mechanism is not essential to creating the stable layer (Nuijens and Emanuel 2018). How these two possible mechanisms explain the presence of the congestus mode across the different Amazon regimes is not obvious. Regimes 1 and 2 are characterized by dry-air intrusions from poleward latitudes, yet exhibit the lowest frequency of congestus; this indicates
385   that other factors are strongly suppressing the vertical development of congestus and cumulonimbus. The higher frequency for congestus during regimes 4 and 5 is accompanied by a greater incidence of organized convection (section 4.3); this suggests the possibility of the stratiform-cooling mechanism. To complicate matters, only the composite soundings for regimes 2 and 5 (as shown in Figure 3) exhibit indications of a mid-level stable layer (~700–550 hPa).

390   Finally, the bulk cloud characteristics as shown in Figure 10 are similar between regimes 4 and 5 during the morning to afternoon hours. However, an important shift in cloud properties under regime 5 is observed during the pre-radiosonde (overnight) periods, with regime 5 associated with more frequent congestus. From such depictions, it is unclear whether this shift in overnight cloudiness in regime 5 is associated with more frequent or resilient congestus, or possible contributions from MCSs. As discussed below, MCSs and/or radar-based indicators for widespread precipitation are more frequent for regime 4.
395   This argues that the increase should be attributed to additional and/or more resilient congestus, and this explanation is consistent with the modest upper (anvil) peak for regime 4 and prominent congestus peak observed for regime 5.

4.2 Differences in Precipitation Behaviors Across Regimes

400   Model evaluation often benefits from precipitation constraints that include comparisons to the diurnal cycle and other precipitation properties. In Figure 11, we plot the diurnal cycle of precipitation from the domain-mean precipitation rate used to constrain the 3-hourly VARANAL products, contingent on the regime-events having measurable precipitation. As in Figure 9, a summary campaign behavior ('all') that includes contributions from days having precipitation at 1200 UTC is also included. For these breakdowns, precipitation rate (in mm/hr) is based on SIPAM estimates for the domain within the 110-km
405   radius of MAO site. The dotted lines on Figure 11 correspond to the domain-mean values, and the shading indicates a 1-sigma standard deviation for regime events. These standard deviations indicate the event-to-event variability; however, precipitation

rates estimated by radar may carry at minimum 30% uncertainty (e.g., bias, or fractional root-mean-square error) owing to miscalibration or other factors (e.g., Xie et al., 2014; Giangrande et al., 2014). Note, the SIPAM rainfall estimates used in VARANAL assume a single radar-rainfall relationship based on disdrometer measurements collected under wet season

410 conditions. This choice implies that the dry season rainfall rates are likely overestimated according to previous Amazon disdrometer studies performed for MAO during wet and dry season precipitation (e.g., Wang et al., 2018).

For radar-derived precipitation rates over the VARANAL domain as in Figure 11, the MAO location favors a pronounced daytime diurnal cycle, with peak occurring after local noon (e.g., 1800 UTC). The well-behaved diurnal cycle is consistent

415 with climatologies over land from the Tropical Rainfall Measurement Mission (TRMM; Nesbitt and Zipser 2003; Yang and Smith 2006; Hirose et al., 2008), but this behavior may be fortuitous, since complex land surface cover, topography, or river / sea-breeze controls influence precipitation measurements in other parts of the Amazon basin and potentially mask a well-defined diurnal cycle (e.g., Adams et al., 2015; Burleyson et al., 2016; Machado et al., 2018). The cloudiest times over the MAO column do not perfectly align with domain-mean precipitation properties, but the times with the most frequent clouds

420 we observe in Figures 9 and 11 are typically near 1800 UTC. Still, there are important shifts between various regimes. For example, regime 5 domain-mean precipitation from 2100 UTC into the overnight hours skews higher than the other regimes and is associated with an increased MAO column cloudiness (e.g., Figure 9e). Overall, moist regimes favor more intense rainfall rates, with the highest rainfall rates observed in regime 4, followed by regime 5. Although fewer clouds, smaller total convective area, and lower domain rainfall rates are observed during the drier season, the individual convective events

425 (updrafts, precipitation) can be quite strong (Giangrande et al., 2016; Machado et al., 2018). This is evident by the relatively high domain-mean rainfall rates that are observed for regimes 2 and 3 for days when precipitation is recorded.

In Figure 12, we plot distributions for the maximum daily radar echo area after 1200 UTC (i.e., largest continuous area from any single radar scan, one assigned per day) occupied by various thresholds for the reflectivity factor, as proxies for deep

430 convective core area coverage ($Z > 40$ dBZ) and widespread rainfall area coverage ($Z > 20$ dBZ). Thus, this measurement is a daily reference to the largest individual cell (any time), not a measurement for the total 'convective' area occupied by cells. Previous studies including Giangrande et al. (2016) and Machado et al. (2018) have indicated that rainy seasons favor larger total convective area coverage. In terms of allowance for singular deeper convective cores (Figure 12a), it is not surprising that regime 4 (e.g., transitional) is associated with the largest convective cells, as based on higher expectations for MCS. In

435 terms of convective core properties associated with $Z > 40$ dBZ behaviors, multiple drier season distributions share comparable behaviors as to regime 5. This is consistent with suggestions that the dry season also promotes isolated, intense convection.

Regimes 4 and 5, in contrast, favor a substantially wider distribution of widespread precipitation coverage as shown in Figure 12b when compared to the drier regimes. An increase in widespread precipitation coverage ($Z > 20$ dBZ) is consistent with

440 the arguments for more ubiquitous weak convection and/or MCS having trailing stratiform anvils (e.g., Romatschke and

13

Houze, 2010). Interestingly, this may be interpreted as weaker cells/precipitation winning out over less frequent, but stronger cells. This is suggested as responsible for the reduced domain-mean precipitation rates compared to regime 2 (Figure 11 reflects only contributions from precipitation events). This view would also be consistent with regime 3 as associated with additional congestus and/or periphery stratiform precipitation, enabled through reduced MUCIN and greater humidity above 600-hPa.

445

4.3 Radar-based Null Event or MCS Event Frequency

In addition to compositing clouds by regime, we explore a simple Bayesian approach to query the likelihood a particular regime promotes different precipitation modes, information that is highly useful for convective parameterization and predictive efforts.
450   If convection initiates for a given regime, what is the likelihood that the convection is nonprecipitating, isolated, or develops to a widespread precipitation event? In Figure 13, we break down the likelihood that precipitation events observed during GoAmazon2014/5 fall under nonprecipitating (NULL), isolated precipitating convection (ISO), and wide deeper convective (WDC) events. Among those WDC events, we identify those events having mature-stage MCS characteristics (i.e., MCS are a subset of the WDC events). For this study, NULL events are defined by a minimum area of $Z > 20$ dBZ that is less than 200
455   km^2. For mature MCS definitions, we follow the guidelines established in Houze et al. (2015) and Feng et al. (2018), where MCS are defined as having continuous 40 dBZ radar echo area exceeding 1000 km^2, with a continuous shield of 20 dBZ radar echo areas exceeding 10000 km^2. WDC events are defined as the precipitation events having a continuous, widespread shield of 20 dBZ echo exceeding 10000 km^2. For simplicity, ISO events are defined as the remaining events that did not fall within NULL or WDC categories (i.e., NULL + ISO + WDC = total events). For the analysis in Figure 13, 595 of the 607 rain-free
460   radiosondes days were also well-observed by the SIPAM.

Overall, NULL precipitation days are rare, accounting for less than 4% of our two-year record (as shown in Figure 13, Table S2). NULL events were predominantly designated during the driest regimes, with regimes 1 and 2 accounting for 20 of the 23 (87%) instances. WDC events account for approximately 21% of the dataset, and commonly observed for regimes 4 and 5
465   (approximately 81%). Subsampling those WDC events, radar-based MCS events are relatively uncommon, accounting for approximately 8% of the dataset. As we plot in Figure 13, the majority of these MCS events were observed during the moist regimes (regimes 4 and 5 accounting for > 70% of the events), with approximately half of all MCSs observed during regime 4. For completeness, the number of MCSs during GoAmazon2014/5 was approximately double those reported, but we have chosen to ignore radar-based MCS that produced rainfall over the MAO site at the time of radiosonde launch. Additional
470   manual inspection of the WDC events also reveals that one-third of WDC events shared MCS-like characteristics, but fell short of study thresholds. Thus, potentially 20% of the campaign period was associated with MCS, although only half are considered for our analysis. Similarly, MCS designations are arbitrary, and we anticipate inconsistencies between this accounting and satellite tracking (e.g., Rehbein et al., 2019). One final consideration is that MCSs do not need to initiate locally (e.g., within the SIPAM radar domain ~ 500 km) to meet our radar-based definitions. We have inspected radar and satellite

14

475 observations for 44/47 MCS events to manually identify MCS from our criteria that initiated to distances >500 km upstream, then propagated over the site. Supplemental Table S2 identifies two MCS categories, 'propagating', and 'local', as reminiscent of previous Amazon studies (e.g., Greco et al., 1990). By our breakdowns, MCS during the drier season are predominantly 'propagating' events, while moist regimes include contributions from both MCS categories.

480 As the regime most associated with mature MCS events, in Figures S8 and S9 we plot composite radiosonde and parameter distributions (MUCAPE, MUCIN) for regime 4 'nonMCS', 'local' (13 events) and 'propagating' events (7 events). In Figure 14, we plot a similar MCS breakdown for 1200 UTC horizontal moisture advection and w from VARANAL. Overall, we do not observe any obvious difference between the composite properties among MCS and nonMCS events within regime 4. Similarities between MCS and nonMCS events are also reflected in the 1200 UTC variational forcing composites shown in

485 Figure 14, with local MCS and nonMCS events reflecting comparable mean conditions. 'Propagating' MCS events are less representative of composite behaviors and suggest weaker thermodynamic conditions with the most favorable large-scale controls. However, these large-scale moisture/velocity enhancements are modest (e.g., vertical velocity increase of 2.5-to-5 hPa/h).

490

5 Summary

To inform on the potential controls for clouds experienced over the Amazon basin, a cluster analysis was performed on routine radiosondes launched during GoAmazon2014/5. This effort follows similar applications of k-means cluster methods that

495 attempt to objectively disentangle larger-scale cloud and precipitation controls from traditional calendar-driven wet/dry season definitions. We identified five primary thermodynamic regimes and explored these states in the context of traditional Amazon definitions, composite large-scale synoptic patterns, and model forcing datasets. Column and scanning radar observations were projected into these states, highlighting the propensities for each state to promote different cloud types, frequencies, and changes to precipitation. Emphasis was given to intra-regime conditions associated with organized convection in the

500 transitional regime (regime 4) most favorable to MCS. Although caution is recommended when considering the findings established over a limited two-year GoAmazon2014/5 deployment, a summary of our key findings are as follows:

- *k*-means clustering of the 1200 UTC radiosonde datasets yields five primary clusters. The three drier regimes relate different states of mid-to-upper level moisture associated with the strength of similar large-scale features that advect

505 colder/drier air into the Amazon basin. The wet to transitional clusters exhibit similar deep moisture thermodynamic profiles, with regime 5 associated with evidence of moisture advection into the Amazon basin from the tropical belt.
- GoAmazon2014/5 cloud frequencies, cloud types and precipitation properties for the five regimes correspond well to bulk changes in the large-scale vertical air motion, moisture advection, local radiosonde thermodynamic composite

15

profile and convective parameter shifts. Most regimes favor frequent clouds and intense precipitation during the early afternoon hours (after 1600 UTC), with precipitation following a single-peak diurnal cycle. These results are consistent with cumulative dataset results from the GoAmazon2014/5 deployment (e.g., Collow et al., 2016; Ghate and Kollias, 2016; Zhuang et al., 2017).

- The moist regimes were associated with modest MUCAPE, reduced MUCIN and higher humidity at all levels. The latter two controls are those suggested as most favorable in the Amazon for more frequent clouds, deeper convection, and widespread stratiform precipitation. These results are consistent with previous studies on the propensity for stronger updrafts during dry or dry-to-wet transitional seasons (e.g., Williams et al., 2002; Giangrande et al., 2016; Wang et al., 2019).

- Regimes 4 and 5 suggest prominent shallow-to-deep cloud transitioning (with trimodal cloud profile behaviors observed in regime 5), with the timing of these transitions potentially contingent on the regime. This later daytime transitioning under regime 5 may suggest the transition has been slowed by the reduced incident solar radiation (more frequent shallow clouds under regime 5), or higher soil moisture values (i.e., smaller Bowen ratio). This transition timing aligns with previous Amazon findings from Zhuang et al. (2017) for 'wet' and 'transitional' season conditions.

- The drier regimes reflect reduced column cloud frequency, bimodal instead of trimodal distributions in vertical profiles of cloud frequency, an absence of mid-level cloud contributions and shallow-to-deep transition signatures, and rainfall properties attributed to weak or isolated (infrequent) deep convection. Although convection is frequently observed during all regimes, dry-season regimes exhibit less-frequent clouds and rare Amazon NULL precipitation events.

- When precipitation is observed, SIPAM radar designations indicate most convection in isolated deeper convective cells. Organized convection was relatively frequent over MAO during this two-year GoAmazon2014/5 deployment (e.g., Rehbein et al., 2019), with approximately 10-20% of the convection observed over MAO associated with MCS. These MCSs were most frequently observed under moist profile conditions (regimes 4 and 5), and over the 1200 UTC to 0000 UTC period, with the best-defined MCSs observed during regime-4 GoAmazon2014/5 periods. Approximately half of the well-defined MCSs that passed over MAO fell outside of the typical diurnal cycle and/or were not associated with regime classifications.

- When considering regime 4 favorability for deep convective events, it is suggested that intra-regime (pre- and post-dry season months) variability may account for shifts in favorability for enhanced storm updrafts and/or electrification. However, this study did not identify shifts in composite thermodynamic profiles or convective parameter distributions between MCS and nonMCS conditions. Additional checks of the large-scale synoptic patterns and forcing datasets under MCS and nonMCS conditions indicate that 'propagating' MCSs may favor an enhancement in the large-scale upward vertical motion (2.5-5 -hPa/h) and moisture tendencies during pre-convective windows that offsets weaker local thermodynamic environments. However, these factors were arguably less important when compared to overall regime 4 proclivity for MCS.

16

Data Availability

545 All ARM datastream to include VARANAL, ARSCL, SONDE and other PI datasets used in this study can be downloaded at http://www.arm.gov and are associated with several "value added product" VAP streams and GoAmazon2014/5 PI datasets. Python machine learning codes were provided by Scikit-learn, as from Pedregosa et al. (2011). Radiosonde visuals were supported by the python package MetPy, as from May et al., (2020). ERA5 reanalysis products (production) are available at: https://www.ecmwf.int/en/newsletter/147/news/era5-reanalysis-production, as from Hersbach and Dee, (2016).

550

570 **References**

Adams, D. K., S. Gutman, K. Holub and D. Pereira, 2013: GNSS Observations of Deep Convective timescales in the Amazon, 2013: Geophysical Research Letters, 40,1- 6, doi:10.1002/grl.50573

Adams, D.K., R.M. Fernandes, K.L. Holub, S.I. Gutman, H.M. Barbosa, L.A. Machado, A.J. Calheiros, R.A. Bennett, E.R.
575 Kursinski, L.F. Sapucci, C. DeMets, G.F. Chagas, A. Arellano, N. Filizola, A.A. Amorim Rocha, R.A. Silva, L.M. Assunção, G.G. Cirino, T. Pauliquevis, B.T. Portela, A. Sá, J.M. de Sousa, and L.M. Tanaka, 2015: The Amazon Dense GNSS

Meteorological Network: A New Approach for Examining Water Vapor and Deep Convection Interactions in the Tropics. *Bull. Amer. Meteor. Soc.,* **96**, 2151–2165, https://doi.org/10.1175/BAMS-D-13-00171.1

Alcântara, C.R., Silva Dias, M.A.F., Souza, E.P., Cohen, J.C.P., 2011. Verification of the role of the low level jets in Amazon squall lines. Atmos. Res. 100, 36–44. https://doi.org/10.1016/j.atmosres.2010.12.023.

Anber, U., Gentine, P., Wang, S. G., and Sobel, A. H.: Fog and rain in the Amazon, P. Natl. Acad. Sci. USA, 112, 11473–11477,2015.

Benedict, J. J., and Randall, D. A.: Observed characteristics of the MJO relative to maximum rainfall. J. Atmos. Sci., 64, 2332–2354, doi:10.1175/JAS3968.1, 2007.

Betts, A. K., Fuentes, J. D., Garstang, M., & Ball, J. H. (2002). Surface diurnal cycle and boundary layer structure over Rondonia during the rainy season. Journal of Geophysical Research, 107(D20), 8065. https://doi.org/10.1029/2001jd000356

Bryan, G.H. and J.M. Fritsch, 2002: A Benchmark Simulation for Moist Nonhydrostatic Numerical Models. *Mon. Wea. Rev.,* 130, 2917–2928.

Burleyson, C. D., Feng, Z., Hagos, S. M., Fast, J., Machado,L. A. T., and Martin, S. T.: Spatial Variability of the Back-ground Diurnal Cycle of Deep Convection around the GoAmazon2014/5 Field Campaign Sites, J. Appl. Meteor. Climatol., https://doi.org/10.1175/JAMC-D-15-0229.1, 2016.

Carvalho, L. M. V., Jones, C., and Liebmann, B.: The South Atlantic Convergence Zone: Intensity, Form, Persistence, and Relationships with Intraseasonal to Interannual Activity and Extreme Rainfall, J. Climate, 17, 88–108, 2004.

Chakraborty, S., Schiro, K. A., Fu, R., and Neelin, J. D.: On the role of aerosols, humidity, and vertical wind shear in the transition of shallow-to-deep convection at the Green Ocean Amazon 2014/5 site, Atmos. Chem. Phys., 18, 11135–11148, https://doi.org/10.5194/acp-18-11135-2018, 2018.

Chakraborty, S., Jiang, J. H., Su, H., & Fu, R. (2020). Deep convective evolution from shallow clouds over the Amazon and Congo rainforests. Journal of Geophysical Research: Atmospheres, 125, e2019JD030962.

Clothiaux, E. E., et al. (2000), Objective determination of cloud heights and radar reflectivities using a combination of active remote sensors at the ARM CART sites, J. Appl. Meteorol., 39, 645– 665.

Cifelli, R., W. A. Petersen, L. D. Carey, S. A. Rutledge, and M. A. F. da Silva Dias, 2002: Radar observations of the kinematic, microphysical, and precipitation characteristics of two MCSs in TRMM LBA. J. Geophys. Res., 107, 8077, https://doi.org/10.1029/2000JD000264.

Collow, A. B. M., M. A. Miller, and L. C. Trabachino (2016), Cloudiness over the Amazon rainforest: Meteorology and thermodynamics, J. Geophys. Res.Atmos.,121, 7990–8005, doi:10.1002/2016JD024848.

Del Genio, A. D.: Representing the sensitivity of convective cloud systems to tropospheric humidity in general circulation models, Surv. Geophys., 33, 637–656, https://doi.org/10.1007/s10712-011-9148-9, 2012.

Drumond, A., Marengo, J., Ambrizzi, T., Nieto, R., Moreira, L., and Gimeno, L.: The role of the Amazon Basin moisture in the atmospheric branch of the hydrological cycle: a Lagrangian analysis, Hydrol. Earth Syst. Sci., 18, 2577–2598, https://doi.org/10.5194/hess-18-2577-2014, 2014.

Fan J, et al. (2018); Substantial convection and precipitation enhancements by ultrafine aerosol particles. Science 359:411–418.

Feng, Z., and Giangrande, Scott. Merged RWP-WACR-ARSCL Cloud Mask and Cloud Type. United States: N. p., 2018. Web. doi:10.5439/1462693.

615   Feng, Z., Leung, L. R., Houze, R. A., Jr., Hagos, S., Hardin, J., Yang, Q., et al. (2018). Structure and evolution of mesoscale convective systems: Sensitivity to cloud microphysics in convection-permitting simulations over the United States. Journal of Advances in Modeling Earth Systems, 10, 1470–1494. https://doi.org/10.1029/2018MS001305.

Findell, K.L.; Eltahir, E.A. Atmospheric controls on soil moisture-boundary layer interactions. Part I: Framework development. J. Hydrometeorol., 4, 552–569, 2003a.

620   Findell, K.L.; Eltahir, E.A. Atmospheric controls on soil moisture-boundary layer interactions. Part II: Feedbacks within the continental United States. J. Hydrometeorol., 4, 570–583, 2003b.

Fu, R. and Zhu, B., and Dickinson, R.: How do the atmosphere and land surface influence the seasonal changes of convection in tropical Amazon?, J. Climate, 12, 1306–1321, 1999.

Gerken, T., Ruddell, B. L., Fuentes, J. D., Araúdo, A., Brunsell, N. A., Maia, J., Manzi, A., Mercer, J., dos Santos, R. N., von

625   Randow, C., and Stoy, P. C.: Investigating the mechanism responsible for the lack of surface energy balance closure in a central Amazonian tropical rainforest. Agr. For. Meteor., 255, 92–103, https://doi.org/10.1016/j.agrformet.2017.03.023, 2018.

Ghate, V.P. and P. Kollias, 2016: On the Controls of Daytime Precipitation in the Amazonian Dry Season. J. Hydrometeor., 17, 3079–3097, https://doi.org/10.1175/JHM-D-16-0101.1

Giangrande, S.E., S. Collis, A.K. Theisen, and A. Tokay, 2014: Precipitation Estimation from the ARM Distributed Radar

630   Network during the MC3E Campaign. J. Appl. Meteor. Climatol., 53, 2130–2147, https://doi.org/10.1175/JAMC-D-13-0321.1

Giangrande, S. E., Toto, T., Jensen, M. P., Bartholomew, M. J.,Feng, Z., Protat, A., Williams, C. R., Schumacher, C., and Machado, L.: Convective cloud vertical velocity and mass-flux characteristics from radar wind profiler observations during GoAmazon2014/5, J. Geophys. Res.-Atmos., 121, 12891–12913, https://doi.org/10.1002/2016JD025303, 2016.

Giangrande, S. E., Feng, Z., Jensen, M. P., Comstock, J. M., Johnson, K. L., Toto, T., Wang, M., Burleyson, C., Bharadwaj,

635   N., Mei, F., Machado, L. A. T., Manzi, A. O., Xie, S., Tang, S., Silva Dias, M. A. F., de Souza, R. A. F., Schumacher, C., and Martin, S. T.: Cloud characteristics, thermodynamic controls and radiative impacts during the Observations and Modeling of the Green Ocean Amazon (GoAmazon2014/5) experiment, Atmos. Chem. Phys., 17, 14519–14541, https://doi.org/10.5194/acp-17-14519-2017, 2017.

Giangrande, Scott. Calibrated Radar Wind Profiler Precipitation Observations and Vertical Velocity Retrievals. United States:

640   N. p., 2018. Web. doi:10.5439/1440997.

Greco, S., Swap, R., Garstang, M., Ulanski, S., Shipham, M., Harriss, R.C., Talbot, R., Andreae, M.O. and Artaxo, P. (1990) Rainfall and surface kinematic conditions over central Amazonia during ABLE 2B. Journal of Geophysical Research: Atmospheres, 95(D10), 17001–17014. https://doi.org/10.1029/JD095iD10p17001.

Hersbach, H. and Dee, D.: ERA5 reanalysis is in production, ECMWF Newsletter, Vol. 147, p. 7, available at:
645   https://www.ecmwf.int/en/newsletter/147/news/era5-reanalysis-production (last access: 14 November 2018), 2016.

Hirose, M., R. Oki, S. Shimizu, M. Kachi, and T. Higashiuwatoko, 2008: Finescale diurnal rainfall statistics refined from eight years of TRMM PR data. J. Appl. Meteor. Climatol., 47, 544–561.

Hohenegger, C., and B. Stevens, 2013: Preconditioning deep convection with cumulus convection. J. Atmos. Sci., 70, 448–464, doi:10.1175/JAS-D-12-089.1

650   Houze, R. A. (2004). Mesoscale convective systems. Reviews of Geophysics, 42, RG4003. https://doi.org/10.1029/2004RG000150.

Houze, R. A. Jr., Rasmussen, K. L., Zuluaga, M. D., and Brodzik, S. R. (2015). The variable nature of convection in the tropics and subtropics: A legacy of 16 years of the Tropical Rainfall Measuring Mission satellite. Reviews of Geophysics, 53, 994–1021. https://doi.org/10.1002/2015RG000488

655   Jensen, M. P., and A. D. Del Genio (2006), Factors limiting convective cloud-top height at the ARM Nauru island climate research facility, J. Clim., 19, 2105–2117.

Jensen, M. P., Toto, T., Troyan, D., Ciesielski, P. E., Holdridge, D., Kyrouac, J., Schatz, J., Zhang, Y., & Xie, S. (2015). The midlatitude continental convective clouds experiment (MC3E) sounding network: Operations, processing and analysis. Atmospheric Measurement Techniques, 8(1), 421–434. https://doi.org/10.5194/amt-8-421-2015.

660   Johnson, R.H., T.M. Rickenbach, S.A. Rutledge, P.E. Ciesielski, and W.H. Schubert, 1999: Trimodal Characteristics of Tropical Convection. J. Climate, 12, 2397–2418.

Jones, A.R.; Brunsell, N.A.: Energy balance partitioning and net radiation controls on soil moisture-precipitation feedbacks. Earth Interact, 13, 1–25, 2009.

Khairoutdinov, M., and D. Randall (2006), High-resolution simulation of shallow-to-deep convection transition over land, J.
665   Atmos. Sci., 63,3421–3436.

Klein, S. A. and Del Genio, A. D.: ARM's Support for GCM Improvement: A White Paper, U.S. Department of Energy, DOE/SC-ARM/P-06-012, Washington, D.C, 2006.

Kousky, V. E.: Pentad outgoing longwave radiation climatology for the South America sector, Revista Brasilera de Meteorología, 3,217–231, 1988.

670   Liebmann, B. and J. Marengo, 2001: Interannual Variability of the Rainy Season and Rainfall in the Brazilian Amazon Basin. J. Climate, 14, 4308–4318.

Löffler-Mang, M., & Joss, J. (2000). An optical disdrometer for measuring size and velocity of hydrometeors. Journal of Atmospheric and Oceanic Technology, 17, 130–139.

Louf, V., Jakob, C., Protat, A., Bergemann, M., & Narsey, S. (2019).The relationship of cloud number and size with their
675   large-scale environment in deep tropical convection.Geophysical Research Letters, 46, 9203–9212.

Machado, L. A. T., Laurent, H., Dessay, N., and Miranda, I.: Sea-sonal and diurnal variability of precipitation over Amazon and its impact on convection over the Amazonia: A comparison of different vegetation types and large scale forcing, Theor. Appl.Climatol., 78, 61–77, https://doi.org/10.1007/s00704-004-0044-9, 2004.

680 Machado, L. A. T., Calheiros, A. J. P., Biscaro, T., Giangrande, S., Silva Dias, M. A. F., Cecchini, M. A., Albrecht, R., Andreae, M. O., Araujo, W. F., Artaxo, P., Borrmann, S., Braga, R., Burleyson, C., Eichholz, C. W., Fan, J., Feng, Z., Fisch, G. F., Jensen, M. P., Martin, S. T., Pöschl, U., Pöhlker, C., Pöhlker, M. L., Ribaud, J.-F., Rosenfeld, D., Saraiva, J. M. B., Schumacher, C., Thalman, R., Walter, D., and Wendisch, M.: Overview: Precipitation characteristics and sensitivities to environmental conditions during GoAmazon2014/5 and ACRIDICON-CHUVA, Atmos. Chem. Phys., 18, 6461–6482, https://doi.org/10.5194/acp-18-6461-2018, 2018.

685 Madden, R. A., and P. R. Julian, 1994: Observations of the 40-50 day tropical oscillation: a review. Mon. Wea. Rev., 122, 814-837.

Mapes, B. E. and Houze, R. A., Jr. (1995) Diabatic divergence profiles in western Pacific mesoscale convective systems. Journal of the Atmospheric Sciences, 52, 1807–1828.

Mapes, B. E., and P. Zuidema (1996), Radiative–dynamical consequences of dry tongues in the tropical troposphere, J. Atmos.
690 Sci., 53, 620–638.

Marengo, J. A., Fisch, G. F., Alves, L. M., Sousa, N. V.,Fu, R., and Zhuang, Y.: Meteorological context of the on-set and end of the rainy season in Central Amazonia during the GoAmazon2014/5, Atmos. Chem. Phys., 17, 7671–7681, 2017.

Martin, S. T., Artaxo, P., Machado, L. A. T., Manzi, A. O., Souza, R.A. F., Schumacher, C., Wang, J., Andreae, M. O., Barbosa, H. M.J., Fan, J., Fisch, G., Goldstein, A. H., Guenther, A., Jimenez, J.L., Pöschl, U., Silva Dias, M. A., Smith, J. N., and
695 Wendisch, M.: Introduction: Observations and Modeling of the Green Ocean Amazon (GoAmazon2014/5), Atmos. Chem. Phys., 16, 4785–4797, https://doi.org/10.5194/acp-16-4785-2016, 2016.

Martin, S.T., P. Artaxo, L. Machado, A.O. Manzi, R.A. Souza, C. Schumacher, J. Wang, T. Biscaro, J. Brito, A. Calheiros, K. Jardine, A. Medeiros, B. Portela, S.S. de Sá, K. Adachi, A.C. Aiken, R. Albrecht, L. Alexander, M.O. Andreae, H.M. Barbosa, P. Buseck, D. Chand, J.M. Comstock, D.A. Day, M. Dubey, J. Fan, J. Fast, G. Fisch, E. Fortner, S. Giangrande, M. Gilles,
700 A.H. Goldstein, A. Guenther, J. Hubbe, M. Jensen, J.L. Jimenez, F.N. Keutsch, S. Kim, C. Kuang, A. Laskin, K. McKinney, F. Mei, M. Miller, R. Nascimento, T. Pauliquevis, M. Pekour, J. Peres, T. Petäjä, C. Pöhlker, U. Pöschl, L. Rizzo, B. Schmid, J.E. Shilling, M.A. Dias, J.N. Smith, J.M. Tomlinson, J. Tóta, and M. Wendisch, 2017: The Green Ocean Amazon Experiment (GoAmazon2014/5) Observes Pollution Affecting Gases, Aerosols, Clouds, and Rainfall over the Rain Forest. Bull. Amer. Meteor. Soc., 98, 981–997.

705 Mather, J. H. and Voyles, J. W.: The Arm Climate Research Facility:A Review of Structure and Capabilities, Bull. Am. Meteor. Soc.,94, 377–392, 2013.

May, P.T. and A. Ballinger, 2007: The Statistical Characteristics of Convective Cells in a Monsoon Regime (Darwin, Northern Australia). Mon. Wea. Rev., 135, 82–92, https://doi.org/10.1175/MWR3273.1

May, R. M., Arms, S. C., Marsh, P., Bruning, E., Leeman, J. R., Goebbert, K., Thielen, J. E., and Bruick, Z., 2020: MetPy: A Python Package for Meteorological Data. Version 0.12.1.post2, Unidata, Accessed 21 April 2020. [Available online at https://github.com/Unidata/MetPy.] doi:10.5065/D6WW7G29.

McFarlane, S. A., Long, C. N., and Flaherty, J.: A climatology of surface cloud radiative effects at the ARM tropical western Pacific sites, J. Appl. Meteorol. Clim., 52, 996–1013, https://doi.org/10.1175/Jamc-D-12-0189.1, 2013.

Mechem, D. B., and Oberthaler, A. J.: Numerical simulation of tropical cumulus congestus during TOGA COARE. J. Adv. Model. Earth Syst., 5, 623–637, doi:10.1002/jame.20043, 2013.

Mechem, D. B., and Giangrande, S. E.: The challenge of identifying controls on cloud properties and precipitation onset for cumulus congestus sampled during MC3E. Journal of Geophysical Research: Atmospheres, 123. https://doi.org/10.1002/2017JD027457, 2018.

Miller, M. A., Nitschke, K., Ackerman, T. P., Ferrell, W., Hickmon, N., and Ivey, M.: The Atmospheric Radiation Measurement Mo-bile Facility, Chapter, AMS Monograph, The first 20 years of ARM, 2014.

Misra, V.: Coupled air, sea, and land interactions of the South American monsoon, J. Climate, 21, 6389–6403,https://doi.org/10.1175/2008JCLI2497.1, 2008.

Nesbitt, S. W., and E. J. Zipser, 2003: The diurnal cycle of rainfall and convective intensity according to three years of TRMM measurements. J. Climate, 16, 1456–1475.

Nuijens, L., and K. Emanuel, 2018: Congestus modes in circulating equilibria of the tropical atmosphere in a two-column model. Quart. J. Roy. Meteor. Soc., 144, 2676–2692. DOI: 10.1002/qj.3385

Pakula, L. and Stephens, G.L. (2009) The role of radiation in influencing tropical cloud distributions in a radiative–convective equilibrium cloud-resolving model. Journal of the Atmospheric Sciences, 66, 62–76.

Parker, M. D., and R. H. Johnson, 2000: Organizational modes of midlatitude mesoscale convective systems. Mon. Wea. Rev., 128, 3413–3436, doi:10.1175/1520-0493(2001)129,3413:OMOMMC.2.0.CO;2.

Peterson, W. A., S. W. Nesbitt, R. J. Blakeslee, R. Cifelli, P. Hein, and S. A. Rutledge, TRMM observations of intraseasonal variability in convective regimes over the Amazon, J. Clim., 15, 1278–1294, 2002.

Pope, M., C. Jakob, and M. Reeder, 2009a: Objective classification of tropical mesoscale convective systems. J. Climate, 22, 5797–5808.

Pope, M., C. Jakob, and M.J. Reeder, 2009b: Regimes of the North Australian Wet Season. J. Climate, 22, 6699–6715, https://doi.org/10.1175/2009JCLI3057.1

Redelsperger, J.-L., D. B. Parsons, and F. Guichard (2002), Recovery processes and factors limiting cloud-top height following the arrival of a dry intrusion observed during TOGA COARE, J. Atmos. Sci., 59, 2438–2457.

Rehbein, A., et al., 2019; https://doi.org/10.1002/joc.6173

Romatschke, U., and R. A. Houze, Jr., 2010: Extreme summer convection in South America. J. Climate, 23, 3761-3791.

Rotunno, R., J. B. Klemp, and M. L. Weisman, 1988: A theory for strong, long-lived squall lines. J. Atmos. Sci.,45, 463–485.

Schumacher, Courtney, and Funk, Aaron. GoAmazon2014/5 Rain Rates from the SIPAM Manaus S-band Radar. United States: N. p., 2018. Web. doi:10.5439/1459578.

Scikit-learn: Machine Learning in Python, Pedregosa et al., JMLR 12, pp. 2825-2830, 2011

745 Sena, E.T., M.A. Dias, L.M. Carvalho, and P.L. Dias, 2018: Reduced Wet-Season Length Detected by Satellite Retrievals of Cloudiness over Brazilian Amazonia: A New Methodology. J. Climate, 31, 9941–9964, https://doi.org/10.1175/JCLI-D-17-0702.1

Sobel, A. H., J. Nilsson, and L. M. Polvani, 2001: The weak temperature gradient approximation and balanced tropical waves. J. Atmos. Sci., 58, 3650–3665.

750 Tanaka, L. M. d. S., Satyamurty, P., & Machado, L. A. T. (2014). Diurnal variation of precipitation in central Amazon Basin. Int. J. Climatol., 34, 3574–3584. https://doi.org/ 10.1002/joc.3929

Tang, S., Xie, S., Zhang, Y., Zhang, M., Schumacher, C., Upton, H., Jensen, M. P., Johnson, K. L., Wang, M., Ahlgrimm, M., Feng, Z., Minnis, P., and Thieman, M.: Large-scale vertical velocity, diabatic heating and drying profiles associated with seasonal and diurnal variations of convective systems observed in the GoAmazon2014/5 experiment, Atmos. Chem. Phys., 16, 755 14249–14264.

Wang, D., Giangrande, S. E., Bartholomew, M. J., Hardin, J., Feng, Z., Thalman, R., & Machado, L. A. T. (2018). The Green Ocean: precipitation insights from the GoAmazon2014/5 experiment. Atmospheric Chemistry and Physics, 18, 9121–9145. https://doi.org/10.5194/acp-18-9121-2018

Wang, D., Giangrande, S. E., Schiro, K., Jensen, M. P., & Houze, R. A. (2019). The characteristics of tropical and midlatitude 760 mesoscale convective systems as revealed by radar wind profilers. Journal of Geophysical Research: Atmospheres, 124, 4601–4619. https:// doi.org/10.1029/2018JD030087

Wang, D., Giangrande, S. E., Feng, Z., Hardin, J.C., & Prein, A.F. (2020). Updraft and Downdraft Core Size and Intensity as Revealed by Radar Wind Profilers: MCS Observations and Idealized Model Comparisons. Journal of Geophysical Research: Atmospheres. doi: 10.1029/2019JD031774

765 Weisman, M.L. and R. Rotunno, 2004: "A Theory for Strong Long-Lived Squall Lines" Revisited. J. Atmos. Sci., 61, 361–382, https://doi.org/10.1175/1520-0469(2004)061<0361:ATFSLS>2.0.CO;2

Williams, E., Rosenfeld, D., Madden, N., Gerlach, J., Gears, N.,Atkinson, L., Dunnemann, N., Frostrom, G., Antonio, M., Bi-azon, B., Camargo, R., Franca, H., Gomes, A., Lima, M., Machado, R., Manhaes, S., Nachtigall, L., Piva, H., Quintil-iano, W., Machado, L., Artaxo, P., Roberts, G., Renno, N.,Blakeslee, R., Bailey, J., Boccippio, D., Betts, A., Wolff, D.,Roy, B., 770 Halverson, J., Rickenbach, T., Fuentes, J., and Avelino, E.: Contrasting convective regimes over the Amazon: Implications for cloud electrification, J. Geophys. Res., 107, 8082,https://doi.org/10.1029/2001JD000380, 2002.

Wright, J.S., Fu, R., Worden, J.R., Chakraborty, S., Clinton, N.E., Risi, C., et al., 2017. Rainforest-initiated wet season onset over the southern Amazon. Proceedings of the National Academy of Sciences, 201621516.

Wu, C.-M., B. Stevens, and A. Arakawa, 2009: What controls the transition from shallow to deep convection? J. Atmos. Sci., 775 66,1793–1806, doi:10.1175/2008JAS2945.1.

Wu, M. and J.-E. Lee, 2019; https://doi.org/10.1029/2019GL082909

Xie, S., Zhang, Y., Giangrande, S. E., Jensen, M. P., Mc-Coy, R., and Zhang, M.: Interactions between cumulus convection and its environment as revealed by the MC3E sounding array, J. Geophys. Res.-Atmos., 119, 11784–11808,https://doi.org/10.1002/2014JD022011, 2014.

780 Xie, Shaocheng, Tang, Shuaiqi, Zhang, Yunyan, and Zhang, Minghua. SCM-Forcing Data. United States: N. p., 2016. Web. doi:10.5439/1273323.

Yang, S., and E. A. Smith, 2006: Mechanisms for diurnal variability of global tropical rainfall observed from TRMM. J. Climate, 19, 5190–5226.

Zermeño–Díaz, D. M., Zhang, C., Kollias, P., and Kalesse, H.: The role of shallow cloud moistening in MJO and non-MJO 785 convective events over the ARM Manus site. J. Atmos. Sci., 72, 4797–4820. doi: 10.1175/JAS-D-14-0322.1, 2015.

Zhang, M. and Lin, J.: Constrained Variational Analysis of Sounding Data Based on Column-Integrated Budgets of Mass, Heat, Moisture, and Momentum: Approach and Application to ARM Measurements, J. Atmos. Sci., 54, 1503–1524, 1997.

Zhuang, Y., Fu, R., Marengo, J. A., and Wang, H.: Seasonal variation of shallow-to-deep convection transition and its link to the environmental conditions over the Central Amazon, J. Geophys.Res. Atmos., 122, https://doi.org/10.1002/2016JD025993, 790 2017.

Zhuang, Y., R. Fu, and H. Wang, 2018: How Do Environmental Conditions Influence Vertical Buoyancy Structure and Shallow-to-Deep Convection Transition across Different Climate Regimes?. J. Atmos. Sci., 75, 1909–1932, https://doi.org/10.1175/JAS-D-17-0284.1
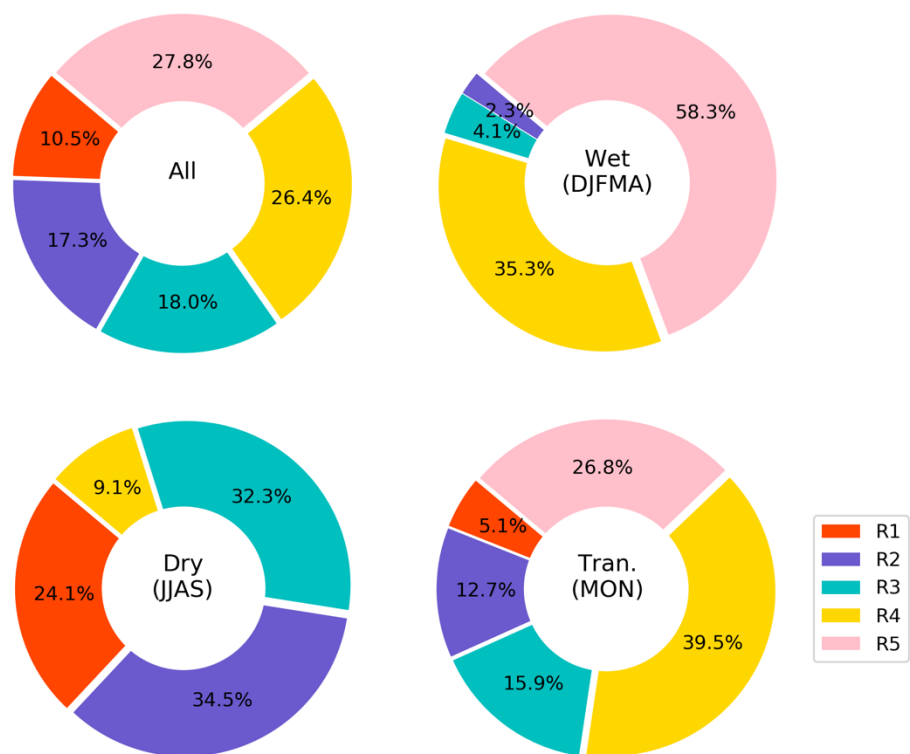
Figure 1. Breakdowns for the frequency to observe regime clusters (regimes 1 through 5 marked as R1 through R5) for the GoAmazon2014/5 radiosonde dataset (1200 UTC), as well as breakdowns for wet season (Dec., Jan., Feb., Mar., Apr.), dry season (Jun., Jul., Aug., Sep.), and transitional season (May, Oct., Nov.) radiosondes.
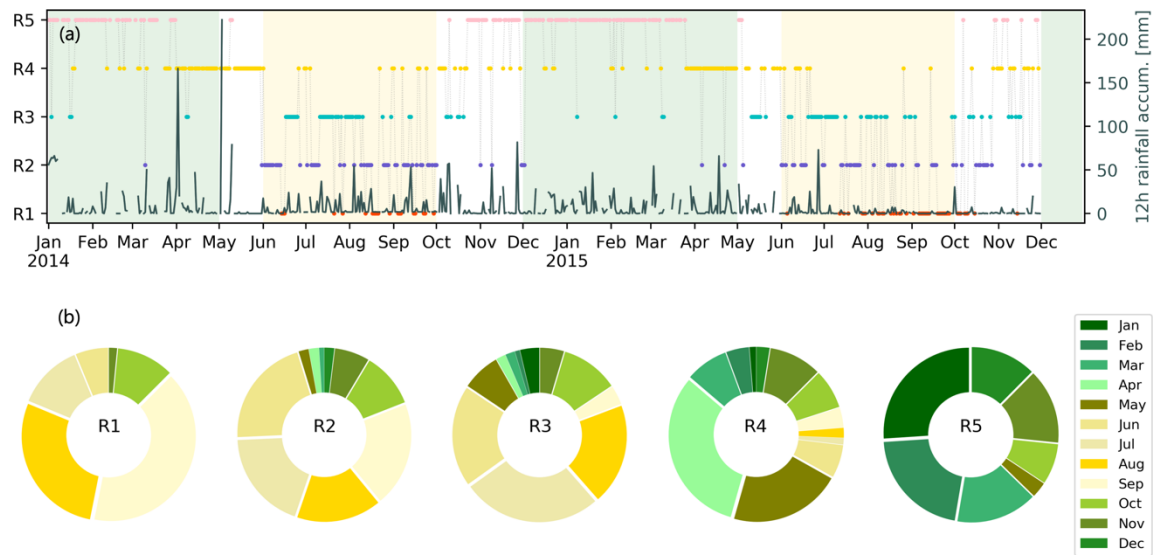
Figure 2. (a) Time series for Amazon regime cluster results (color-coded as also in Figure 1) with corresponding 12h (1200 UTC - 00 UTC) rainfall accumulation (from the MAO rain gauge). The green shading indicates the wet seasons and the yellow shading indicates the dry seasons according to calendar definition; (b) Relative breakdown for the frequency of each regime according to month.
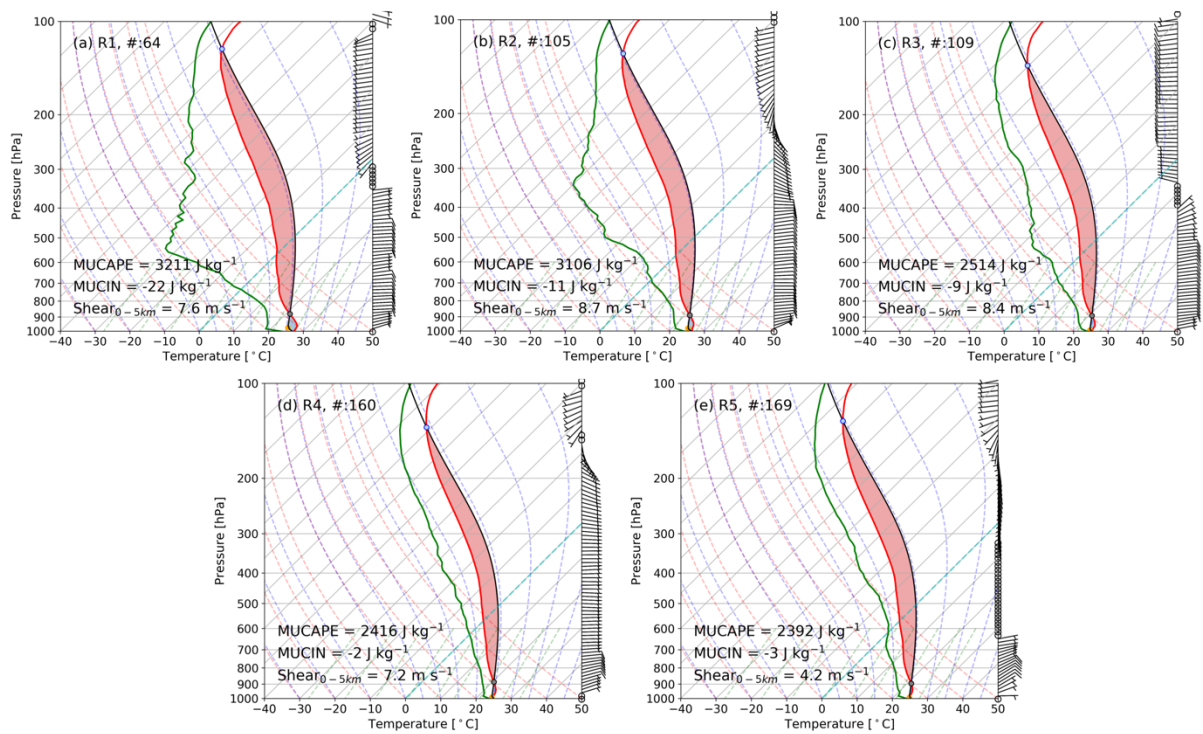
Figure 3. Composite 1200 UTC radiosondes for each regime. MUCAPE, MUCIN, and wind shear (surface to 5 km) parameters report regime-median values.
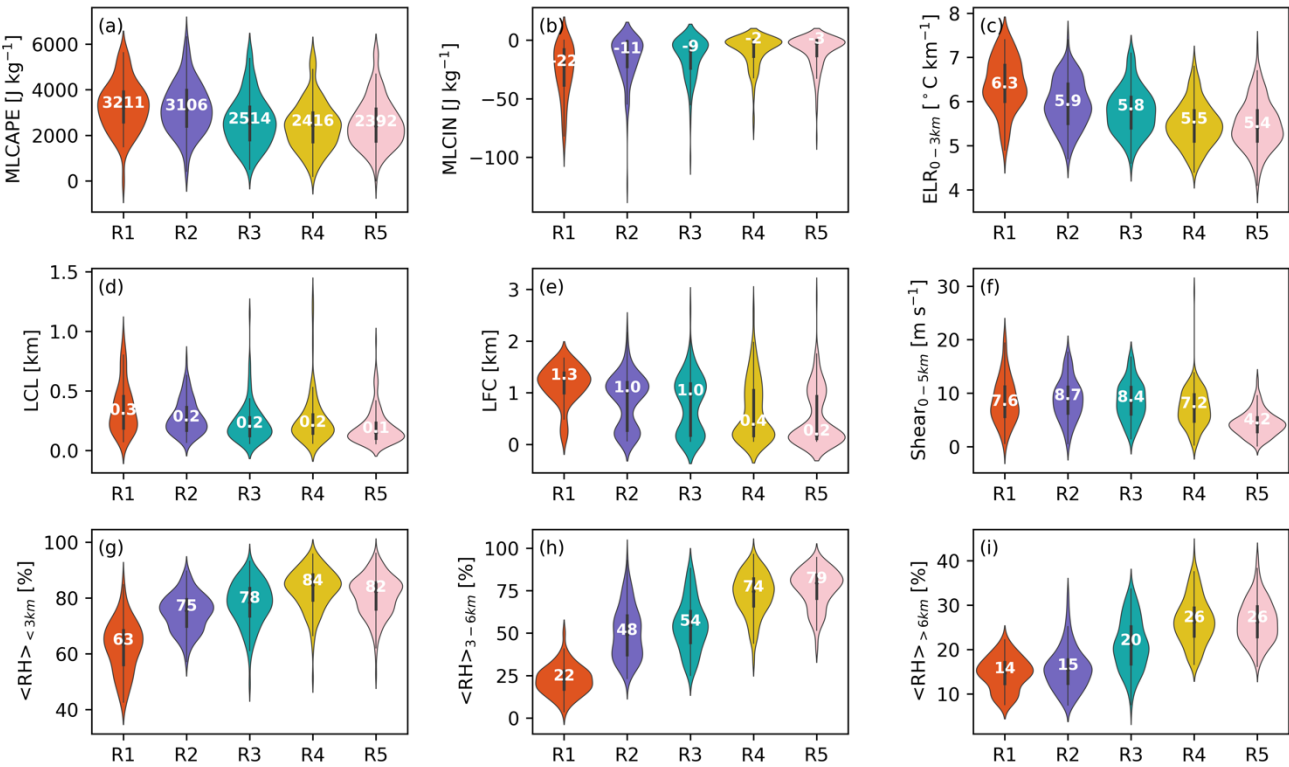
860 **Figure 4.** Shaded probability density plots for select thermodynamic quantities of interest estimated from the 1200 UTC radiosonde in each Amazon regime. The median values for each regime distribution are reported on each violin (white text). The interior black box shows the interquartile range and the thin black lines reflect the 95% confidence interval.
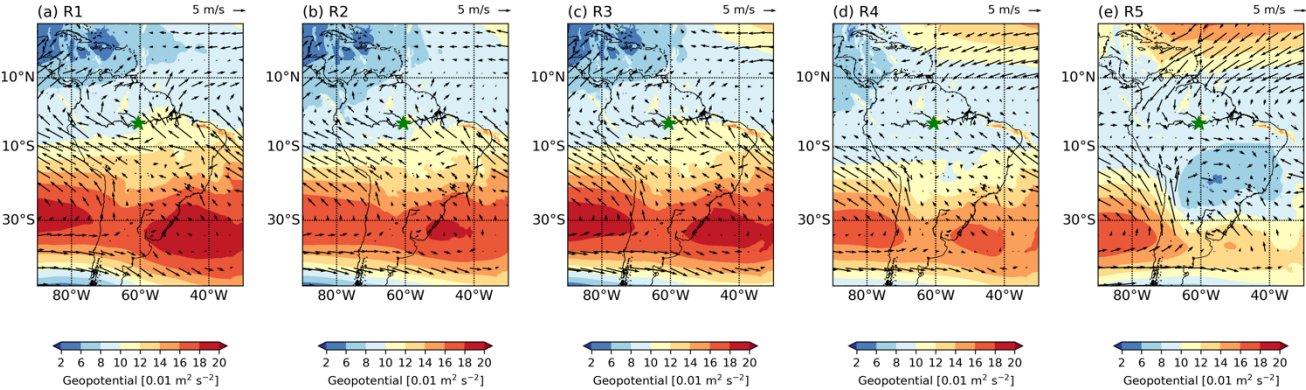
Figure 5. Composite large-scale synoptic patterns (geopotential heights in color [0.01 m2 s-2] and horizontal winds) projected into each regime, as from ERA5 for the 1000-hPa level. The green star indicates the ARM MAO site.
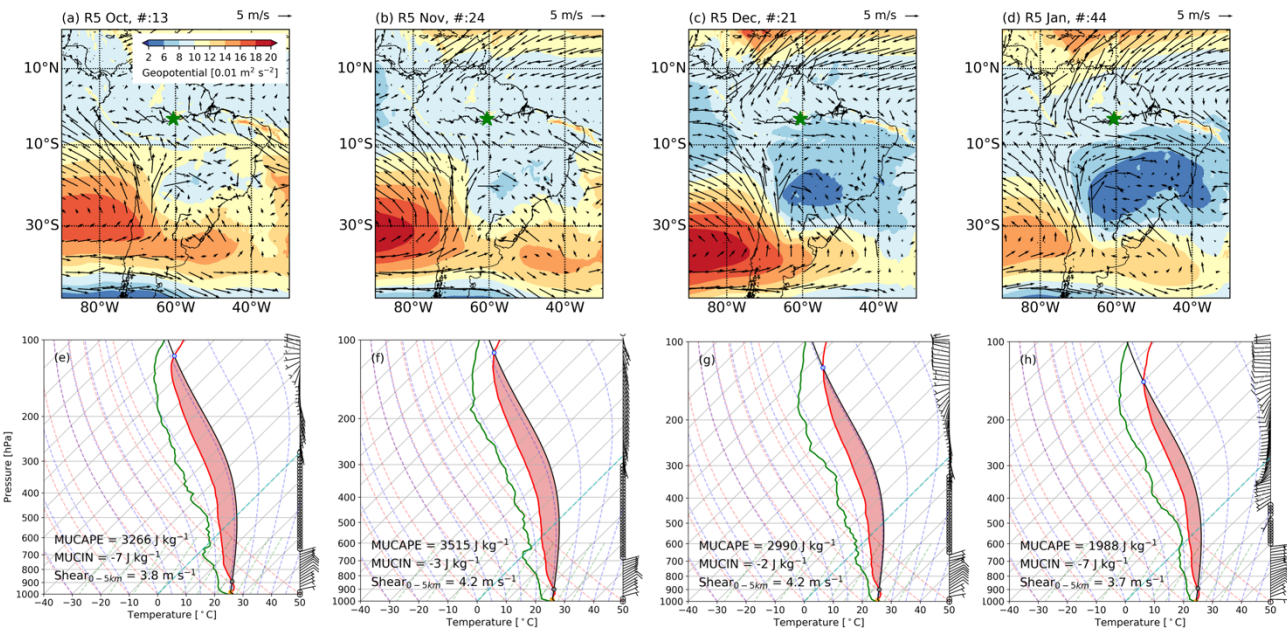
880

Figure 6. Composite monthly large-scale synoptic patterns at 1000 hPa (following Figure 5) and radiosondes, associated with regime 5. Plots correspond left-to-right to (a) October, (b) November, (c) December, and (d) January.
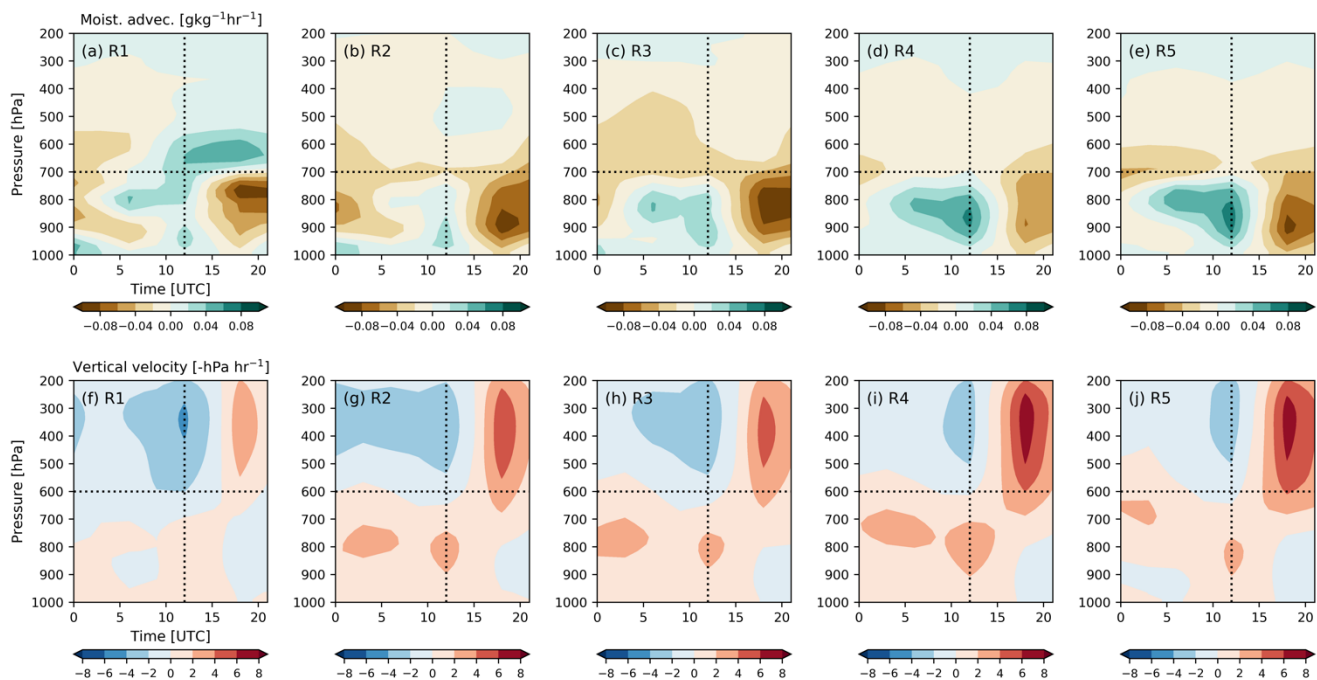
Figure 7. Composite diurnal (UTC) large-scale SCM variational forcing dataset (VARANAL) fields for (a-e) regime breakdowns of the horizontal moisture advection (green = positive moisture advection), and (f-j) large-scale background vertical velocity (red = upward vertical motion). 1200 UTC columns and 600-hPa (f-j)/700-hPa(a-e) levels are highlighted as dotted lines.
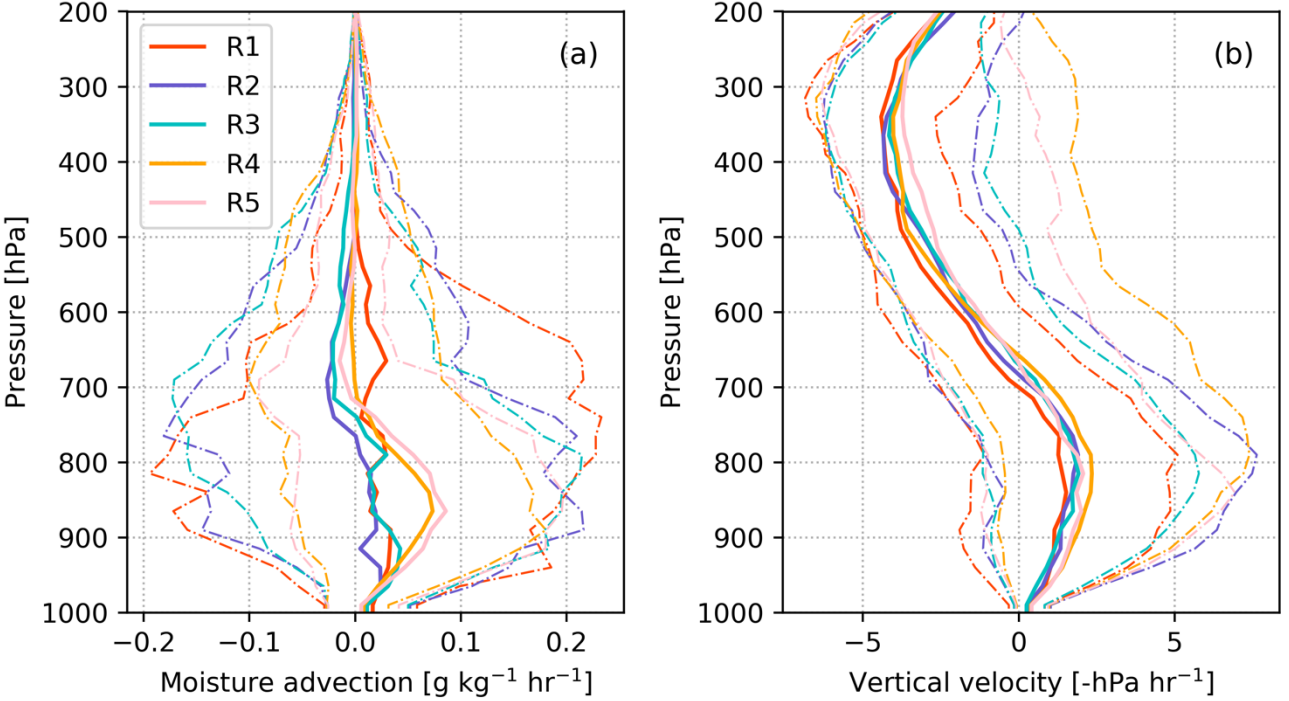
Figure 8. Median profiles (thick solid lines) of (a) horizontal moisture advection and (b) large-scale background vertical velocity (positive value = upward motion) for each regime at 1200 UTC. The 10th and 90th percentile ranges for the variational analysis fields are represented by the dashed-dotted lines.

940

945

950

955
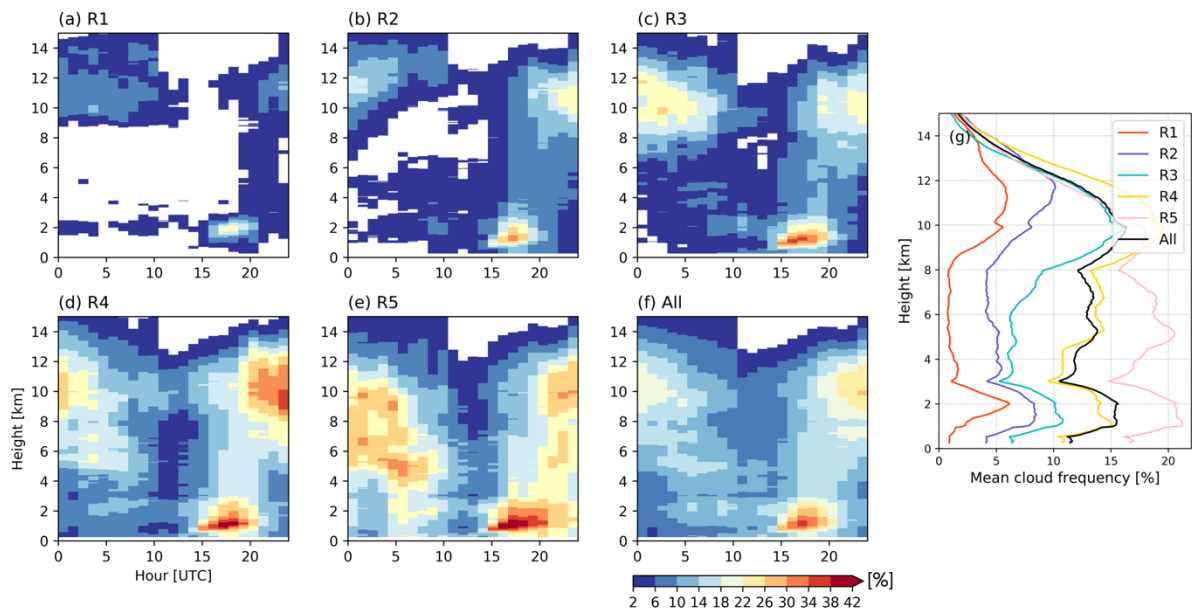
Figure 9. The diurnal cycle of hour-mean cloud frequency (when cloud coverage > 2%) as a function of height for each regime (a-f), as according to a multi-instrument cloud profiling retrieval. The mean 1h cloud frequency profiles are shown in (g).

970

975

980

985

33
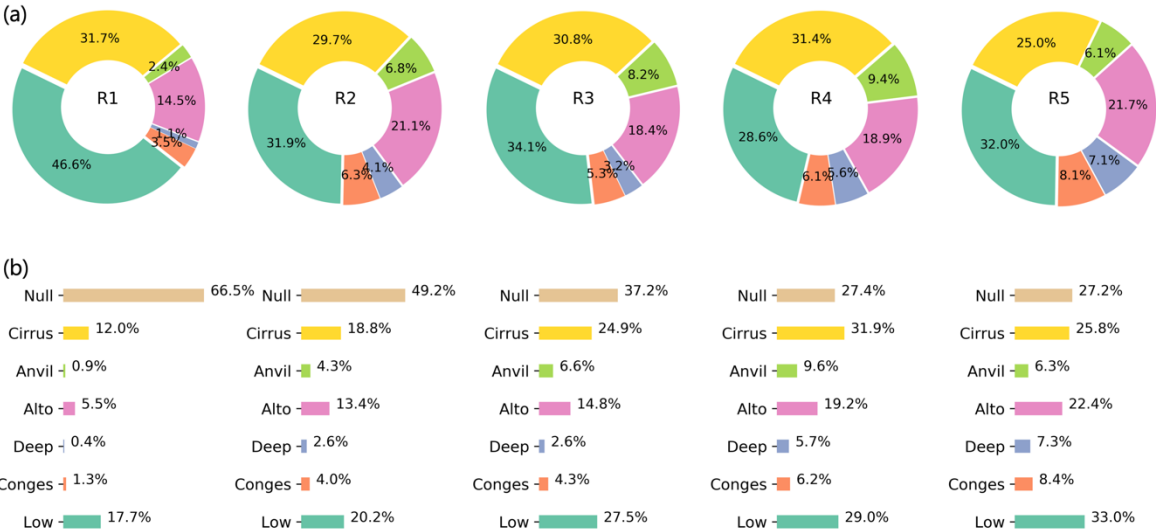
Figure 10. (a) Relative frequency of occurrence for specific cloud types in the column above the ARM MAO site for regime periods between 1200 UTC and 0000 UTC, and (b) percentages when compared to cloud-free conditions.
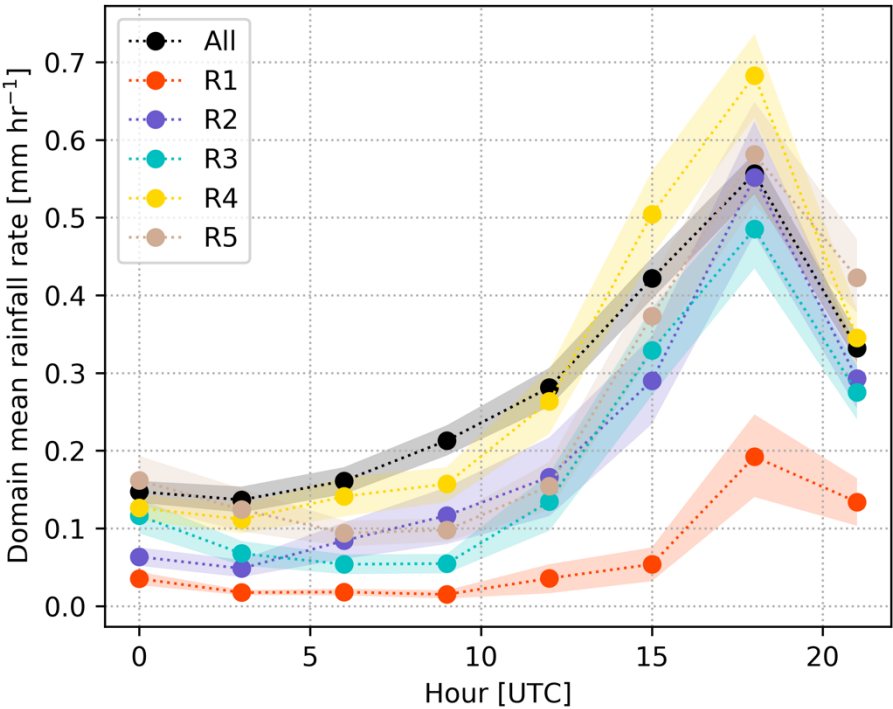
Figure 11. Domain-mean precipitation rate (for events with measurable precipitation) from the SIPAM radar to within a 110 km radius of the MAO site. The dotted lines report the dataset mean values, and the shading is 1-sigma standard deviation.
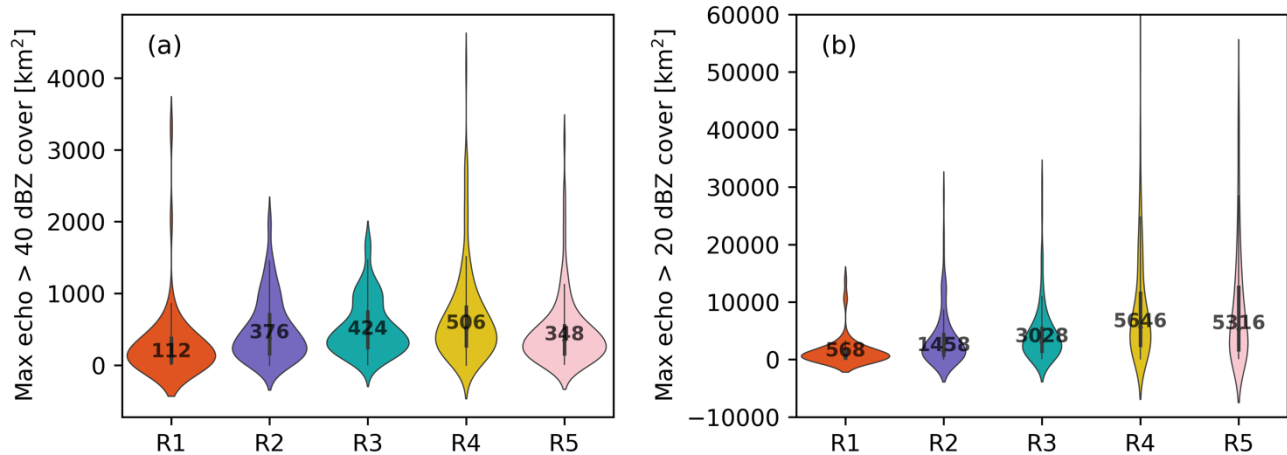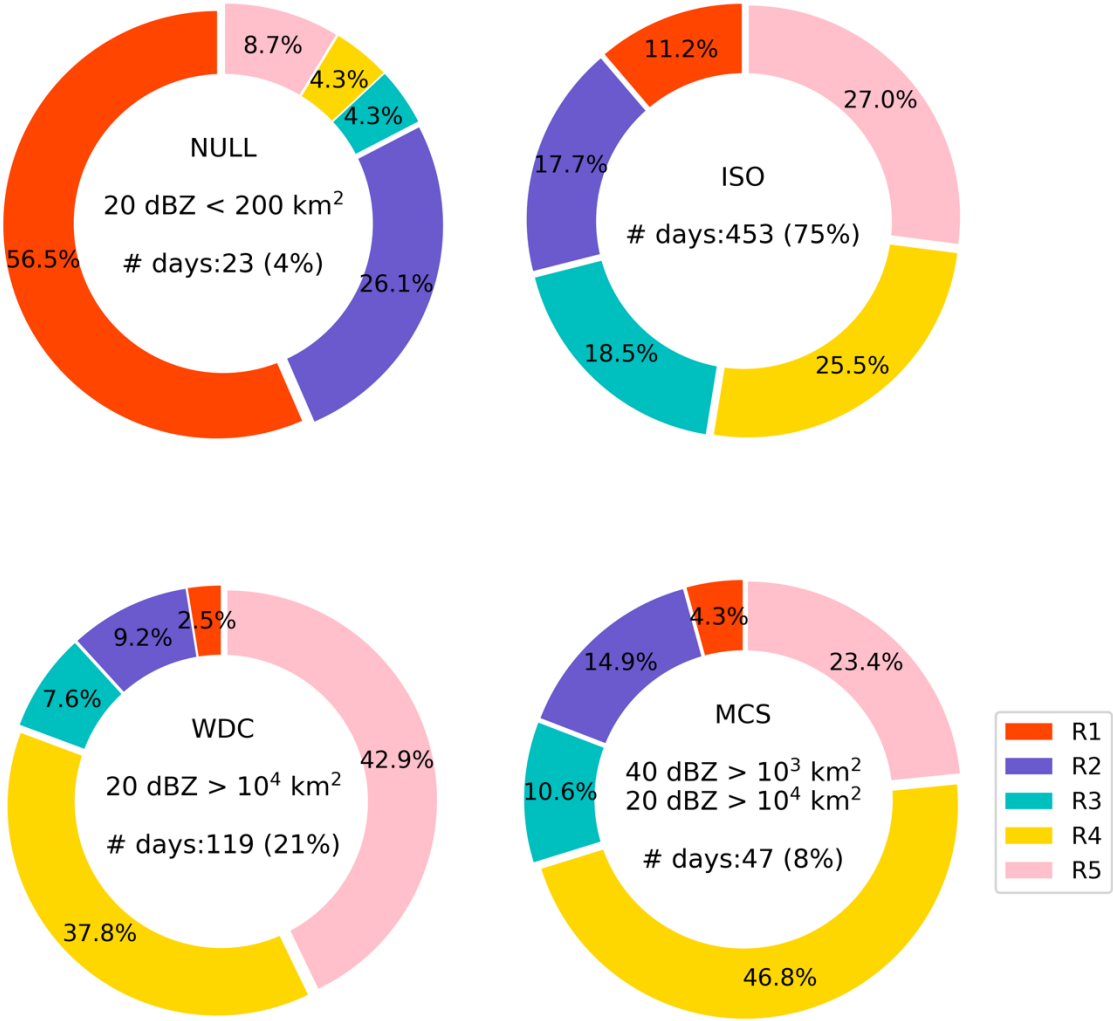
1020

Figure 12. As in Figure 4, the maximum contiguous 2 km CAPPI radar echo coverage [in km^2] for any radar scan within a regime day that is occupied by radar echoes exceeding an intensity (a) Z > 40 dBZ, or (b) Z > 20 dBZ, for hours between 1200 UTC and 0000 UTC that day.

Figure 13. As in previous frequency plots, but for the percentage of (top left) NULL, (top right) ISOlated, (bottom left) wide deep convection (WDC) and (bottom right) MCS days associated with each regime cluster.
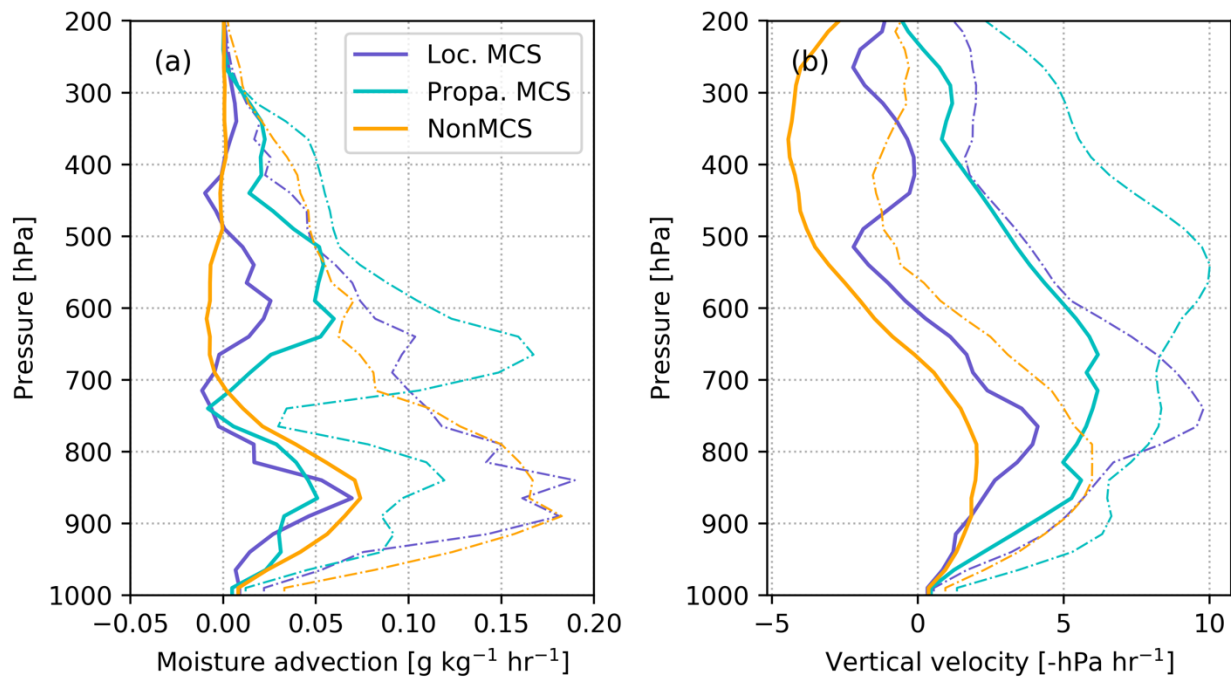
Figure 14. Variational forcing profiles at 1200 UTC for nonMCS, local MCS, and propagating MCS cases with rain rate less than 1.5 mm/hr. Profiles correspond to the regime 4 conditions. Solid lines are median profile values and dashed lines are the 95th percentile values.